Validation of Satellite-based Rainfall Estimation over the Limpopo Basin

by

Mussa Mustafa

A thesis submitted in partial fulfilment of the requirements for the Degree of Master of Science in Agricultural Meteorology

Supervisors

Barnabas Chipindu
(University of Zimbabwe)

and

Petrus J. M. Visser
(South African Weather Service)

University of Zimbabwe

Faculty of Science

June 2007

Abstract

The main objective of this study was to validate satellite-based rainfall estimation algorithms over the Limpopo Basin. The satellite rainfall estimation was done using four algorithms which combine infrared and passive microwave data. These are Climate Prediction Centre (CPC) Morphing (CMORPH), Multiple Precipitation Analysis (MPA), Precipitation Estimation Remotely Sensed Information using Neural Network (PERSIANN), and Naval Research Laboratory Blended (NRLB) methods. The validation was done by comparing satellite rainfall estimates with daily gauge data collected from Botswana, Mozambique, South Africa and Zimbabwe and three-daily moving area average rainfall with three-daily gauge data during 2005/2006 rainfall season. The gauge data were averaged into grid boxes of 0.25^o x 0.25^o resolution, using the inverse weighting interpolation method and the satellite estimates were developed using pixel by pixel at resolution of 0.25^o. A surface mask was used over the Limpopo Basin.

A variety of validation statistics were used to measure different aspects of each algorithm quality, based on contingency tables, and threshold rain of 1 mm/day. All the algorithms showed some skill in estimating rainfall with coefficients of determination ranging from 0.528 to 0.69. Both CMORPH and MPA algorithms exhibited high values of coefficient of determination. The values ranged from 0.5495 to 0.7767 by moving the daily area average rainfall to every three days. The statistical results showed that the CMORPH algorithm performed better than the other three methods. All satellite estimation methods overestimated rainfall with a positive bias which ranged from 0.2 to 0.3. The mean absolute error and root-mean square error ranged from 2.5 – 5.2 and 5.7 – 8.9 mm/day, respectively. The errors were caused by the sparse rain gauge network quality of rain gauge data and inadequacy in the satellite estimation algorithms. The Heidke skill score ranged from 0.19 to 0.28.

The study concluded that CMORPH performed better than the other techniques although all methods overestimate rainfall in the region. The satellite rainfall estimation algorithms can perform better if there is improvement of rainfall measurement infrastructure and data exchange within the Limpopo Basin between the four countries.

To my late parents, and

To my wife Ester,

daughter Adaima and son Junior.

Acknowledgements

Table of Contents

List of Tables

List of Figures

List of Appendices

Glossary of Acronyms

AIP	Algorithm Inter-comparison Project
AMSU	Advanced Microwave Sounding Unit
AMSR	Advanced Microwave Scanning Radiometer
ANN	Artificial Neural Network
AVHRR	Advanced Very High Resolution Radiometer
CCD	Cold Cloud Duration
CERES	Clouds and Earth's Radiation Energy System
CMORPH	Climate Prediction Centre Morphing
CPC	Climate Prediction Centre (of the USA)
CSAV	Cloud System Advection Vector
CSI	Critical Success Index
CST	Convective-Stratiform Technique
DMSP	Defence Meteorological Satellite Programme
ESC	Earth Satellite Corporation
ETS	Equitable Threat Score
EUMETSAT	European Organization for Exploitation of Meteorological Satellites
FAR	False Alarm ratio
FOV	Fields of View
FTP	File Transfer Protocol
GARP	Global Atmospheric Research Program
GATE	GARP Atlantic Tropic Experiment
GMS	Geostationary Meteorological Satellite
GMSRA	GOES Multispectral Rainfall Algorithm
GOES	Geostationary Operational Environmental Satellite
GOS	Global Observing System
GPCP	Global Precipitation Climatology Project
GPI	GOES Precipitation Index
GTS	Global Telecommunication System
HKS	Hanseen and Kuipers Score
HRV	High Resolution Visible channel
HSS	Heidke Skill Score
HQ	High Quality
IDL	Interactive Data Language
INAM	Instituto Nacional de Meteorologia (Mozambique)
IR	Infrared channel
ITCZ	Inter-Tropical Convergence Zone
LAM	Linhas Aéreas de Mozambique (Mozambique Airline Company)
LEO	Low Earth-Orbiting
LIS	Lightning Imaging Sensor
METEOSAT	Geostationary Meteorological Satellite of EUMETSAT
MPA	Multiple Precipitation Analysis
MPA-RT	Real-time Multi-Satellite Precipitation Analysis
MSG	Meteosat Second Generation
MW	Microwave
NASA	National Aeronautical and Space Administration
NASDA	National Space Development Agency (of Japan)
NESS	National Earth Satellite Service
NIR	Near Infrared channel
NOAA	National Oceanic and Atmospheric Administration

NRLB	Naval Research Laboratory
PERSIANN	Precipitation Estimation from Remotely Sensed Information using ANN
PI	Precipitation Index
PIP	Precipitation Inter-comparison Project
PMW	Passive Microwave
POD	Probability of Detection
POES	Polar-orbiting Operational Environmental Satellite
PR	Precipitation Radar
RMSE	Root - Mean Square Error
SAWS	South African Weather Service
SEVIRI	Spinning Enhanced Visible and Infrared Imager
SI	Scattering Index
SPE	Satellite Precipitation Estimates
SSM/I	Special Sensor Microwave Imager
TAMSAT	Tropical Applications of Meteorology using Satellite Data
TIR	Thermal Infrared channel
TMI	TRMM Microwave Imager
TRaP	Tropical Rainfall Potential
TRMM	Tropical Rainfall Measuring Mission
TSDIS	TRMM Science Data and Information System
UAGPI	Universally Adjusted GPI
UNDP	United Nations Development Programme
USA	United States of America
UTC	Universal Time Coordinate
UZ	University of Zimbabwe
VAR	Variable Rain Rate
VIRS	Visible and Infrared Radiometer System
VIS	Visible channel
VISSR	Visible and Infrared Spin Scan Radiometer
WMO	World Meteorological Organization
WWW	World Weather Watch
WV	Water Vapour

Chapter 1   INTRODUCTION

1.0   Introduction and General Context of the Problem

Water is one of the most abundant substances in the earth-atmosphere system and it is fundamental to the sustenance of most human and animal life.

In many parts of Africa, where the agriculture is rainfed, inadequate rainfall can mean crop failure and famine while too much rainfall can lead to devastating floods. For instance, Mozambique experienced drought conditions in 1998 and severe flooding in 2000 and 2001 (Layberry *et al.*, 2006). The floods of 2000 also affected Malawi, South Africa, and Zimbabwe, but in Mozambique the impact of the phenomenon was more severe than in other countries. About 700 hundred people were reported to have died, 145 thousand hectares of various crops were washed away and some 90% of irrigation infrastructure were damaged or destroyed. The assessment carried out by World Bank indicated that the direct and indirect costs of damages amounted to 450 million United States dollars (International Reconstruction Conference, 2000).

Determining the spatial and temporal distribution of rainfall is necessary for the management of water resources and for flood forecasting. It is also an essential component of any scientific investigation of the hydrologic cycle, the global water balance and large-scale global atmospheric modelling.

Historically, the areal estimation of rainfall has been accomplished by use of rain gauges distributed over particular catchments (WMO, 1996). The rain gauge is a relatively simple instrument which samples the rain by capturing rain drops continuously over a fixed time interval. Rainfall amount is specified as the depth (mm) to which a flat horizontal impermeable surface would have been covered if no water were lost by run-off, evaporation or percolation.

The major shortcoming of this instrumentation is that the measurement is only at certain points. It has been well documented that rainfall is highly spatial and temporal variability (Arkin and Janowiak, 1993). Although there are a vast number of rainfall gauges world-wide, they are not adequate to define the rainfall input for most needs.

According to WMO (1996), a representative gauge density is one gauge every 15 km^2, a condition rarely met by most hydro-meteorological services. The result of this is that most rainfall events are not recorded especially in the Limpopo basin where most of the rainfall is convective. With a good network of rain gauges it is possible to map rainfall over small areas but this approach is not practical for large areas, remote land areas of the globe or for oceans. The quantitative estimation of precipitation is a problem of major importance, especially in the tropics due to the significant role of tropical precipitation in the global energy budget and the atmospheric general circulation (Jobard and Desbois, 1992).

Although a conventional rain gauge network gives rainfall observations at a daily time scale, throughout much of the African continent the network is inadequate both in terms of spatial and temporal coverage, while radar, a remote sensing instrument, is generally not a feasible proposition due to cost and inadequate infrastructure (Grimes e*t al*., 2003).

Recognizing the practical limitations of rain gauges, scientists have increasingly turned to remote sensing as a possible means for quantifying the rainfall input to the globe. It should be stressed, however, that remote sensing is at present, and will continue as a supplement to, rather than a replacement for, more traditional methods of rainfall assessment. The measurement of rainfall by rain gauges is fraught with some problems, but those relatively simple instruments will long continue to provide the data against which rainfall assessments by other means must be adjusted. Satellites measure an integral of space at a point in time. Visible and infrared techniques derive qualitative or quantitative estimates of rainfall from satellite imagery through indirect relationships between energy reflected by clouds (or cloud brightness temperatures) and measured precipitation. A number of methods have been developed and tested during the past 20 years with a measured degree of success (WMO, 1996).

Satellite-based rainfall estimation is needed to address issues such as rainfall occurrence, amount and distribution at all temporal scales for a number of applications in meteorology, climatology, hydrology and environmental sciences.

In order to use these rainfall estimates appropriately it is essential to know of their accuracy and expected error characteristics. This is done by validating the satellite

precipitation estimates against "ground truth" from rain gauge and/or radar observations, but time and space scales have to be matched.

1.1   Objectives

1.1.1   Main objective

The main objective of this study is to investigate the use of satellite rainfall estimation methods over the Limpopo River Basin.

1.1.2   Specific objectives

The specific objectives are:

- to carry out a literature survey of existing methods of rainfall estimation using satellites;
- to generate daily rainfall estimates over the Limpopo Basin using satellite-based rainfall estimation methods, and
- to validate the satellite-based rainfall estimates over the Limpopo Basin.

1.2   Potential Benefits of the Research

The Limpopo basin stretches across Botswana, Mozambique, South Africa and Zimbabwe. Effective management of this basin is important for all countries. This has already been recognized by the creation of the Limpopo Commission between the countries to facilitate sustainable development within the basin. Natural events, such as droughts, floods have direct impacts on the economies of member countries. This interdependency is further recognized by creation of two Trans-frontier Game Parks between Mozambique, South Africa and Zimbabwe.

The monitoring of rainfall over the Limpopo Basin is very important in order to prevent losses of flora and fauna due to floods and/or drought. Since the region is very large, the use of remote sensing to obtain rainfall estimation needs to be investigated. This will establish a critical foundation for the improved sustainable management of the basin.

1.3   Thesis Layout

This thesis is composed of 5 chapters. Chapter 1 contains the introduction and relevant information on rainfall measurement problems, and alternative ways to overcome them. The chapter includes the main and specific objectives of the study together with the potential benefits of the research. Relevant background on meteorological satellites and literature review on satellite-based rainfall estimation methods are presented in Chapter 2. Details of material and methods used in the study are described in Chapter 3. These include the study area, satellite data sources and processing, and the validation methodology. The discussion of the results is presented in Chapter 4. Finally, the conclusions and recommendations are outlined in Chapter 5.

Chapter 2   LITERATURE REVIEW

2.0   Introduction

A satellite is any object that orbits another object. Weather satellites are satellites that are primarily used to monitor earth's weather and climate. There are many operational meteorological satellites that can be used for monitoring the weather over different parts of the globe. The satellites have different spatial and temporal resolutions and provide a stream of invaluable data in support of operational meteorology and many other disciplines. In recent years, the applications of these satellites have grown far beyond the dreams of those who designed and operated the systems. One of the applications of weather satellites is the monitoring of precipitation. Several satellite precipitation algorithms have been developed to estimate rainfall from visible, thermal infrared (TIR) and microwave radiation using satellite imagery (Barrett, 1970).

This chapter provides a background on meteorological satellites and a summary of various satellite-based rainfall estimation methods.

2.1   Background on Meteorological Satellites

Meteorological satellites measure radiation coming from the earth and its atmosphere. This radiation may be reflected solar radiation i.e. by the surface, clouds, water vapour and aerosols, or it may be terrestrial radiation emitted by the earth's surface, atmosphere and clouds. The earth's atmospheric gases are affected differently by different wavelengths of radiation. Meteorological satellites have been designed to take advantage of these responses to observe different aspects of the earth and its atmosphere (Harries, 2000). The radiometer is the instrument used to measure the intensity of the radiant energy received in a specific wavelength band. When the radiometer collects a certain amount of energy it registers a count, which is proportional to the intensity of the radiation received. The relationship between radiation and counts is established by the radiometer's calibration. The area viewed by the radiometer is called a footprint and its total radiation is assigned to a pixel centred at the middle of the footprint. In order to build an image of earth of a reasonable size, a scanning system is employed to physically change the direction in which the radiometer is pointing. A complete image

is built up when all the pixels in the image have been assigned a value by the radiometer (Rao *et al.,* 1990).

There are two kinds of meteorological satellites, geostationary and polar-orbiting. Geostationary meteorological satellites orbit the equator at the same rate the earth spins and hence they remain at nearly an altitude of about 36000 km above one point on the equator. This position allows continuous monitoring of a specific region. Geostationary meteorological satellites are also important because they use a "real time" data system, meaning that the satellites transmit images to the receiving system on the ground as soon as the sensor takes the picture (Schmetz *et al*., 2002). Successive cloud photographs from these satellites can be put into a time-lapse movie sequence to show the cloud movement, dissipation, or development associated with weather fronts and storms. This information is a great help in forecasting the progress of large weather systems. The observation area of a geostationary satellite is limited within its field of view, and the information of its imagery is useful in the area between 70° N and 70° S (EUMETSAT, 1998). The main advantages of geostationary satellites are that they observe the earth from a fixed position above the equator and they can be used to monitor the change of meteorological phenomena including cloud motion of tropical cyclones and/or depressions at short time intervals.

Polar-orbiting satellites closely parallel the earth's meridional lines. These satellites pass over the north and south polar regions on each revolution. As the earth rotates to the east beneath the satellite, each pass monitors an area to the west of the previous pass. Eventually, the satellite covers the entire globe. Polar-orbiting satellites have the advantage of photographing clouds directly beneath them (EUMETSAT, 1998). Thus, they provide sharp pictures in polar regions, where photographs from a geostationary meteorological satellite are distorted because of the low angle at which the satellite "sees" this region. In any period of 24 hours each polar satellite can view the entire planet, once during daylight and once at night (Schmetz *et al*., 2002). Polar orbiters also circle the earth at a much lower altitude (about 850 km) than geostationary meteorological satellites and provide detailed photographic information about objects, such as violent storms and cloud systems (Ahrens, 2000). The polar satellites carry a much wider variety of instrumentation than the geostationary satellites and can observe the planet in far more details, but less frequency.

The whole globe can be effectively observed by the good/dense combination of observing system composed of both geostationary and polar orbiting meteorological satellites (Figure 2.1). The combination of the geostationary, polar orbiting and Tropical Rainfall Measuring Mission meteorological satellites makes up the space segment of the Global Observing System (GOS) under the World Weather Watch (WWW) program promoted by the World Meteorological Organization (WMO) (EUMETSAT, 1998).
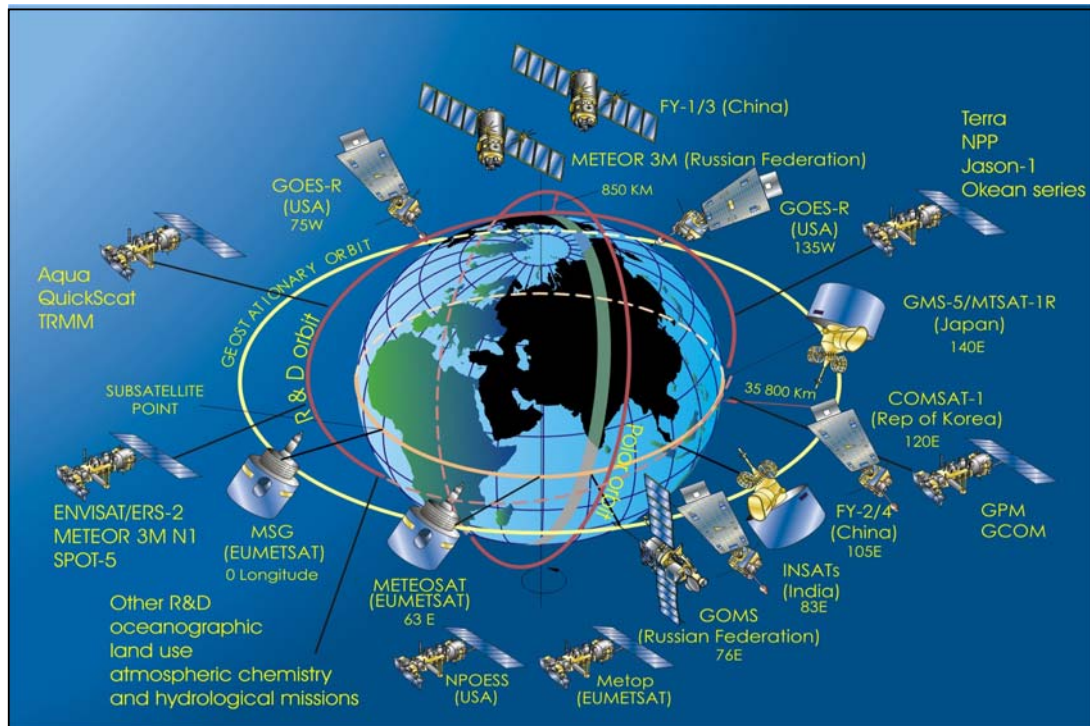
Figure 2.1: Global system of meteorological satellites in 2003.
(Source: www.eumetsat.org, 2007)

Advances in satellite-based remote sensing have enabled scientists to develop precipitation estimates having near-global coverage, thereby providing data for regions where ground-based networks are sparse or unavailable (Sorooshian *et al.,* 2000). However, this advantage is offset by the indirect nature of the satellite observables (e.g., cloud-top reflectance or thermal radiance) which have then to be related to surface precipitation amount (Petty and Krajewski, 1996).

In general, satellite-based precipitation estimation algorithms use information from two primary sources. The visible (VIS) and infrared (IR) channels from geosynchronous satellites are used to establish a relationship between cloud-top conditions and rainfall rates at the base of the cloud. This relationship can be developed at relatively high spatial (4 km x 4 km) and temporal resolution (30 minutes).

7

The first imaging sensors aboard meteorological satellites measured radiation in the VIS band (0.4 – 0.7 μm). VIS imagery generally offers the highest spatial resolution and provides a view of the earth that closely matches our senses (Stanley and Thomas, 1995). Land, clouds, and ocean are easily discernible. The obvious limitation to VIS data is that they are available only from the sunlit portion of the earth, as effectively data is lost during night time.

The IR channels are most often between 1 and 30 μm. The most common IR band for meteorological satellites is in the 10 – 12.5 μm window, in which the atmosphere is relatively transparent to radiation upwelling from the earth surface. When the word infrared is used alone to describe an image, it is nearly always in the 10 – 12.5 μm window rather than in another portion of the electromagnetic spectrum. IR radiation is related to the temperature of the emitting body and because of that the troposphere generally cools with night and it helps to interpret the atmospheric processes occurring within the scene. An important characteristic of the IR channels is their ability to provide images at night. This provides continuous coverage of cloud evolution over a full 24 – hour period (Stanley and Thomas, 1995).

Microwave is an electromagnetic radiation having wavelengths between approximately 1×10^3 μm and 1×10^6 μm (corresponding to 0.3 and 300-GHz frequency) bounded on the short wavelengths side by far infrared and on the long wavelength side by very high frequency radio waves. Passive systems operating at these wavelengths are sometimes called passive microwave systems. The microwave (MW) channels from low-orbiting satellite are used to more directly infer precipitation rates by penetrating the cloud, but a low-orbiting satellite can retrieve only one or two samples per day from one area. Microwave radiation is sensitive to an array of surface and atmospheric parameters, including precipitation, cloud water, water vapour, water droplets phase, soil moisture, surface temperature, atmospheric temperature and ocean surface wind speed.

The relative strengths and weaknesses of various sources (Yilmaz *et al*., 2005) have been exploited in the development of algorithms that combine and make the best use of each source.

2.1.1 Meteosat Second Generation

Meteosat Second Generation (MSG) is a European geostationary meteorological satellite launched in 22 August 2002 operated by European Organization for Exploitation of Meteorological Satellites (EUMETSAT). MSG is spin stabilized and capable of greatly enhanced earth observations (Schmetz *et al.*, 2007). The satellite has a 12 – channel imager, known formally as the spinning enhanced visible and infrared imager (SEVIRI). This radiometer has eight spectral channels in the thermal infrared (TIR), three channels in the visible (VIS) spectrum and a broadband high resolution on visible channel (www.eumetsat.org). The eight TIR channels and three VIS channels have a sampling resolution of 3 km at nadir and scan the full disk of the earth (www.eumetsat.org). The high resolution VIS channel provides images with 1 km sampling at nadir. Data rate limitations confine the high-resolution VIS images to half the earth in an east-west direction (EUMETSAT, 2004). Table 2.1 shows characteristics of MSG 12 channels spectrum and the main observational applications.

Table 2.1: Characteristics of Meteosat Second Generation

Channel No	Spectral Band (μm)	Characteristics of spectral band (μm)	Main observational application
1	VIS0.6	0.56 – 0.71	Surface, clouds, wind fields
2	VIS0.8	0.74 – 0.88	Surface, clouds, wind fields
3	NIR1.6	1.50 – 1.78	Surface, cloud phase
4	IR3.9	3.48 – 4.36	Surface, clouds, wind fields
5	WV6.2	5.35 – 7.15	Water vapour, high level clouds, atmospheric instability
6	WV7.3	6.85 – 7.85	Water vapour, atmospheric instability
7	IR8.7	8.30 – 9.10	Surface, clouds, atmospheric instability
8	IR9.66	9.38 – 9.94	Ozone
9	IR10.8	9.80 – 11.80	Surface, clouds, wind fields, atmospheric instability
10	IR12.0	11.00 – 13.00	Surface, clouds, atmospheric instability
11	IR13.4	12.40 – 14.40	Cirrus cloud height, atmospheric instability
12	HRV	0.40 – 1.10	Surface, clouds

(Source: EUMETSAT, 1998)

2.2 Satellite-based Rainfall Estimation Methods

Precipitation estimation methods are divided into four categories, based on whether they use the following data:

i)   visible and infrared,

ii)   passive microwave,

iii)   radar, and

iv)   combined infrared and microwave data.

2.2.1 Visible and Infrared Techniques

The development of visible (VIS) and infrared (IR) techniques has a long history and relies upon the relationship between cloud top characteristics and the rainfall falling from the cloud. Although this relationship can be somewhat tenuous many techniques have been developed. One of them is the geostationary operational environmental satellite (GOES) precipitation index (GPI) (Arkin and Meisner, 1987). The technique relies upon the fraction of cloud colder than 235 K in the IR with a fixed rain rate. This method provides a useful benchmark by which to assess other algorithms. More complex algorithms have been developed with varying degrees of success. Recent techniques have included the operational GOES IR rainfall estimation technique, or auto-estimator (Vicente *et al*., 1998, 2001) and the GOES multispectral rainfall algorithm (GMSRA) (Ba and Gruber, 2001). The auto-estimator utilises data from the GOES 10.7 µm channel through a regression against radar to generate rainfall estimates, while the GMSRA uses all five channels from the GOES instrument. Information provided by the growth rate of clouds and the spatial gradients is used to discriminate between rain clouds and non-raining cirrus clouds, with the GMSRA incorporating cloud-top particle information.

Both techniques use an additional moisture correction factor to account for evaporation of rain falling from the clouds and not reaching the surface. According to Ba and Gruber (2001), correlations between the surface data and the auto-estimator were slightly less than that of the GPI but substantial improvements are seen in the bias and root-mean square error (RMSE).

Similar improvements were seen with the GMSRA not only in the RMSE and bias, but also the correlation (Vicente *et al*., 1998; Ba and Gruber, 2001).

Visible and infrared techniques are grouped together because they share a common characteristic: the radiation does not penetrate through the cloud. VIS and IR techniques estimate precipitation falling from the bottom of the cloud based on radiation coming from the top and/ or the side of the cloud, depending on viewing geometry. According to Stanley and Thomas (1995), VIS and IR precipitation estimation schemes are necessarily indirect; a cloud's brightness or equivalent blackness temperature may be related to the rain falling from it, but the raindrops themselves are not directly sensed.

Early research using data from polar-orbiting satellites (prior to the era of geostationary satellites) pursued a wide range of avenues, including relating 3-hour precipitation probability to IR window brightness temperatures (Lethbridge, 1967), estimating daily rainfall from visible (Follansbee, 1973) and IR (Follansbee and Oliver, 1975) data, and estimating monthly rainfall based on nephanalyses (charts of cloud type and coverage) constructed from polar-orbiting satellite overpasses (Barrett, 1970).

The advent of geostationary satellites made VIS/IR-based satellite precipitation estimates (SPEs) useful for operational evaluation of extreme-precipitation events, because the time interval involved (15 minutes at present) is much more compatible with the time scale of these events than the time interval between the overpasses of a polar-orbiting satellite (Scofield and Kuligowski, 2003). This dramatic increase in the availability of IR and VIS imagery was accompanied by a similarly dramatic increase in the number of techniques for retrieving precipitation estimates from these data. The more notable algorithms include the so-called Griffith–Woodley technique (Griffith *et al*., 1978); the GOES precipitation index (Arkin and Meisner, 1987), and the convective–stratiform technique (Adler and Negri, 1988). Many of these algorithms were initially developed for large time and space scales, but the scales have become finer as instrumentation has improved and the data-processing capacity has increased.

In this vein, Scofield and Oliver (1977) pioneered the first operationally applied meso-scale storm algorithms that could be modified for a variety of extreme weather situations (Borneman, 1988). A fairly recent development has been the development of SPE algorithms that use artificial neural network techniques, which provide a flexible

framework for using information about cloud spatial characteristics instead of simply relying on brightness temperature values alone.

The main weakness of VIS/IR-based techniques is that they infer the surface rainfall from the cloud-top characteristics. However, more direct measurements of rainfall are possible with algorithms utilizing passive microwave (PMW) data. Barrett and Martin (1981) divide visible and infrared techniques into five categories: cloud indexing, life history, bispectral, cloud model techniques and artificial neural networks.

2.2.1.1   Cloud – indexing technique

This technique was the first to be developed to estimate rainfall from space. It is based on the assumption that the probability of rainfall over a given area is related to the amount and type of cloudiness present over this area (Stanley and Thomas, 1995). The approach is, therefore, to perform a cloud structure analysis (objective and subjective) based on the definition of criteria relating cloudiness to a coefficient (or index) of precipitation. The general approach for cloud indexing methods involving infrared observations is to derive a relationship between a precipitation index (PI) and a function of the cloud surface area, $S[T_b]$, associated with the background brightness temperature, T_b [K] colder than a given threshold temperature, To [K]. This relation is generally expressed as:

$$PI = A_o + \sum_i A_i . S_i \left[T_b \right]$$
(2.1)

for T_b < To

where A_o (mm/h) and A_i (mm) are constants to be determined empirically.

The most widely used of these algorithms is the GPI in which a rainfall amount of 3 mm is associated with each hour of cold cloud duration (CCD) [A_o = 0 mm, A_1 = 3 mm/h in Eq. (2.1)]. For the GPI, the temperature threshold is normally taken as 235 K (Grimes *et al.,* 2003). Although the GPI gives good results over tropical oceans, it is known to overestimate rainfall amounts over the land. The following problems are associated with the technique:

- the bias created by the potential presence of high-level non-precipitating clouds such as cirrus;

- the satellite measurements represent instantaneous observations integrated over space while rain gauge observations are integrated over time at a given site, and

- the relationships derived for a given region and period of time may not be applicable for a different region and season.

Other problems include difficulties in defining rain/no rain boundaries and inability to cope with the rainfall patterns at the meso or local scales.

One of the first methods of rainfall estimation using this principle was developed by Follansbee at National Earth Satellite Service (NESS) in the United States of America (USA). It was the first method to use the National Oceanic and Atmospheric Administration (NOAA) polar-orbiting satellite data, and it assumes the following relationship:

$$R = \frac{K_1 A_1 + K_2 A_2 + K_3 A_3}{A_o}$$

(2.2)

where R is average rainfall across the broad study area for each 24 hour period; A_o is the area under study; A_1, A_2 and A_3 are areas of A_o covered by the three most important types of rain-producing clouds (cumulonimbus, cumulus congestus, and nimbostratus); and K_1; K_2 and K_3 are empirical coefficients. This method therefore only considered convective clouds in the low latitudes. To take into account the diurnal variability of cloud in rain in these low latitudes, the equation was simplified to:

$$R = \frac{K_1 A_1}{A_o}$$

(2.3)

Empirical rainfall intensity weights are applied to these percentages (Rao *et al.,* 1990): 1.0 for cumulonimbus, 0.25 for nimbostratus and 0.02 for cumulus congestus. Visible and infrared pictures are used to determine the cloud types and the percentages of the area occupied by each type. Local climatologies can be used to adapt the weighting factors to specific areas.

2.2.1.2   Bispectral techniques

This techniques relies on the assumption that clouds that are bright in visible images are much more likely to precipitate than dark clouds because brightness is related to optical depth and thus to cloud thickness. Clouds that are cold in infrared images are more likely to precipitate than warm clouds because cold clouds have higher tops than warm clouds (Stanley and Thomas, 1995). Bispectral methods attempt to combine these rules by considering that clouds which have the best chance of raining are both cold and bright (Lethbridge, 1967). Lesser amounts (lower probabilities) of precipitation can be expressed from cold-but-dark clouds (cirrus) and bright-but-warm clouds (stratus).

2.2.1.3   Life-history techniques

The approach is based on the observation of a series of consecutive images obtained from a geostationary satellite (WMO, 1996). Life-history techniques take into account a cloud's life cycle. As with most satellite techniques, life-history techniques go back to the earliest days when the necessary data became available. The interval between consecutive pictures must be short. An example is the Wisconsin method developed by Stout *et al.* (1979) who related volumetric rain rate (R_v) to cumulonimbus cloud area and areal change for estimation of tropical oceanic convective rainfall by the relationship:

$$R_v = a_0 A + a_1 \frac{dA}{dt}$$
(2.4)

where A is the cloud area at time t, and a_0 and a_1 are empirically determined coefficients. The basis of this method is the observation that plots of area and volumetric rain rate for particular clouds show similar shapes, but cloud area lags behind rainfall. Implied here is the condition that there exists a threshold which defines an area closely related to production of rain. The coefficients are normally calculated from combining measurements by least squares regression of satellite cloud area on radar volumetric rain rate, Barrett and Martin (1981). Problem with this method is how to get instantaneous real-time values of rainfall (Stout *et al*, 1979). Coefficients used in this method are given in Table 2.2.

Table 2.2: Regression Coefficients

Band	a_0 (m/s)	a_1 (m)
Visible	5.2×10^{-7}	2.6×10^{-3}
Infrared	5.4×10^{-7}	2.8×10^{-3}

(Source: Stanley and Thomas, 1995)

It has been observed that the amount of precipitation associated with a given area cloud is also related to its stage of development, therefore, two clouds presenting the same aspect (from the VIS/IR images point of view) may produce different quantities of rain depending on whether they are growing or decaying (Rao *et al.*, 1990).

Using half-hourly GOES data in the global atmospheric research programme (GARP) Atlantic tropic experiment (GATE) area, Stout *et al.* (1979) adopted a threshold count of 172 to define rain clouds in the visible channel, and 160 for clouds with temperatures of about 250 K in the infrared (Stanley and Thomas, 1995).

A widely applied precipitation-estimation technique is the Griffith-Woodley technique (Griffith *et al.*, 1976; Woodley *et al.*, 1980). This is a diagnostic method for estimating rainfall over large areas (10^4 to 10^5 km^2) and for long time scales (12 to 24 hours) by the use of VIS and IR GOES imagery. Its algorithm is based on the knowledge that areas of active convection and rainfall, mainly in the tropics, are brighter (colder) than other areas in VIS (IR) pictures. The algorithm uses hourly imagery.

To estimate the precipitation from single cloud, the cloud-defined as anything colder than 253 K – is first followed for its entire lifetime to determine its maximum areal extent. Clouds that merge or split are determined, and the resulting clouds are treated as new clouds. The major advantage of this method is that it can be automated, and the weakest part of the technique seems to be the process of tracking clouds throughout their lifetimes before assigning precipitation.

2.2.1.4   Cloud model techniques

To improve precipitation estimation techniques based on VIS and IR satellite data, it is believed that it is necessary to build the theory of the physics of the cloud into the retrieval process. One way to do this is through the use of cloud models (Stanley and Thomas, 1995).

The earliest such attempt was by Gruber (1973), who noted that Kuo's (1965) parameterization of convection could be used to relate fractional cloud cover to rain rate. Another use of cloud is in adjusting calibration coefficients. Most of the above techniques were developed in a particular location. The changes necessary to apply them elsewhere are not obvious, according to Stanley and Thomas (1995). Wylie (1979) attempted to use the one-dimensional cloud model and adjusted the satellite rain estimates and obtained substantially improved results.

The convective-stratiform technique (CST) is an example of the cloud model technique and uses the IR (10.5 - 12.6 μm channel) imagery from the GOES to identify thunderstorm cloud tops and assign corresponding rain rates (Adler and Negri, 1988). Minima in the brightness temperatures are determined to be convective centres (thunderstorms). The average rain rate over the rain area of a cell is based on calculations using volume rainfall rates and dividing by the convective rain area. The rain rates are assigned in a spiral fashion, from the convective centre outward until the calculated areal extent is filled.

Adler and Mack (1984) studied the ability of a one-dimensional cloud model to explain differences in cloud top temperature-rain rate relationships in Florida and Oklahoma. Adler and Negri (1988) applied the results of Adler and Mack (1984) in a tropical precipitation estimation scheme that they called the convective-stratiform technique (CST). The technique can be applied in four ways.

Firstly, a one-dimension cloud model is run using a actual movement representative sounding as input. The outputs are (1) a relationship between cloud top temperature and rain rate and (2) a relationship between cloud top temperature and raining area.

Secondly, IR satellite data are analysed. Local minima in the IR temperatures are found and screened to eliminate thin, non precipitating cirrus. The remaining minima are assumed to be convective elements protruding from the top of cirrus anvils. Around each convective element the modal temperature in an area approximately 80 km on all sides is calculated. The average of all anvil temperatures is used as a threshold for stratiform precipitation.

Thirdly, precipitation is assigned to the convective elements. The rain rate and raining area are determined from the cloud-top temperature using the output of one-dimension cloud model. To map the rain, the calculated rain rate is assigned to pixels in a spiral fashion. Starting at the centre of the temperature minimum, and continuing until the raining area is reached.

Finally, to every point that is colder than the stratiform threshold and that did not receive any convective precipitation, a 2 mm/h stratiform rain rate is assigned.

The Scofield and Oliver method (Scofield and Oliver, 1977) is another approach of the cloud model technique that uses GOES infrared and high-resolution visible images to make half-hourly or hourly rainfall estimates for deep convective systems of tropical air masses. Estimates of convective rainfall are computed by comparing the changes in cloud character that are observed between two consecutive images of enhanced IR and high-resolution VIS data. The Scofield and Oliver method is quite different from other visible-infrared techniques in that it is not automated.

2.2.1.5   *Artificial Neural Network techniques*

An artificial neural network (ANN) provides a computationally efficient way of determining an empirical, possibly nonlinear relationship between a number of ''inputs'' and one or more ''outputs.'' In addition, the ANN has been shown to be effective in extracting significant features from noisy data and for this reason the most common applications have been in the field of pattern recognition. For more detailed description of neural networks see Grimes *et al.* (2003).

Many studies have been performed using an ANN approach in atmospheric science (Hsieh and Tang, 1998). In the field of remote sensing, an ANN approach has also been used by Aires *et al.* (2001) for retrieval of surface temperature and atmospheric water vapour from satellite data. Recently ANN algorithms for rainfall monitoring have been successfully applied by Hsu *et al.* (1997), Tsintikidis *et al.* (1997), and Bellerby *et al.* (2000). In the case of the **p**recipitation **e**stimation from **r**emotely **s**ensed **i**nformation using **a**rtificial **n**eural **n**etworks (PERSIANN) system described by Hsu *et al.* (1997), the inputs are satellite thermal infrared temperatures and their spatial derivatives plus a parameter that classifies the underlying surface as land, sea, or coast. The algorithm was then adapted to use passive microwave data (Sorooshian *et al.*, 2000).

The neural network is used to discriminate between rain rates of different cloud patterns via a ''self-organizing feature map.'' A big improvement was noticed if the network was continually updated by calibration against available real-time infrared data. Sorooshian *et al.* (2000) reported that good results could be achieved by real-time updating with tropical rainfall measuring mission (TRMM) precipitation radar. Tsintikidis *et al.* (1997) compared an ANN approach with linear regression for rainfall estimation over the ocean from special sensor microwave imager (SSM/I) passive microwave data and found that the ANN performed better than the regression for the same input.

In the method described by Bellerby *et al.* (2000), the input parameters are brightness temperatures and their spatial derivatives for three IR and one VIS sensor on the GOES geostationary satellite. The output is the instantaneous rain rate. Calibration and validation was carried out using TRMM precipitation radar data, and the method was shown to perform consistently better than a locally calibrated GPI technique.

2.2.2   Passive Microwave techniques

Satellite passive microwave (PMW) data provide a direct method for rainfall estimation through the emission-based retrieval of atmospheric liquid water over ocean or scattering-based retrieval of precipitation ice above the freezing level over land or ocean. Unfortunately the passive microwave techniques have poorer spatial resolution due to longer wavelengths than IR techniques (Visser *et al.*, 2004) and low temporal resolution for they are usually flown on polar orbiters. Therefore, it is not useful for

short-term precipitation estimations, unless combined with geostationary IR or other orbiting data.

Although the high spatial and temporal resolution of VIS/IR data from geostationary satellites make them ideally suited for SPE, the relationship between rainfall rate and the characteristics of the cloud tops is indirect and is best suited for convective precipitation, for which the cloud-top height and cloud depth are somewhat related.

These difficulties have led to a body of research into using microwave data to produce SPEs (Scofield and Kuligowski, 2003). Information about cloud thickness and water/ice content can be inferred from microwave radiances because only heavily precipitating clouds are optically thick in the microwave spectrum. This is done using one of two approaches. Emission algorithms compare the emissions of cloud water at low microwave frequencies with the values that would be expected if no cloud were present, which is best done over a radiometrically cold surface such as the open ocean, so that clouds appear to be warm. Scattering algorithms estimate the backscattering of upwelling microwave radiation by ice particles in the clouds by comparing the (low) cloud brightness temperature with the relatively high values that would be observed if no cloud were present.

Early work using the emission approach included that of Weinman and Guetter (1977), who used 37-GHz data from the electrically scanning microwave radiometer on the Nimbus-6 satellite. Spencer (1986) developed a more quantitative algorithm for 37-GHz data from the scanning multichannel microwave radiometer on Nimbus-7. The advent of the SSM/I and, in particular, its introduction of an 85.5-GHz channel led to the development of scattering algorithms that were much more robust over land than were emission algorithms and resulted in substantial improvements in the ability to estimate rainfall from microwave radiance data (e.g. Barrett *et al.*, 1988; Spencer *et al.*, 1989).

Despite the time limitations of observations from polar-orbiting satellites, Ferraro *et al.* (2000) have demonstrated that microwave-based SPEs are useful for meso-scale storm analysis and forecasting. However, the most useful application appears to be in using microwave SPEs in conjunction with GOES data. TRMM also offers an opportunity to investigate the use of multiple instruments in conjunction for SPE, because the TRMM satellite carries not only the TRMM microwave imager (TMI) but also a precipitation

radar, VIS and IR sensors, and a lightning detector. Microwave SPEs have also proven to be useful as a basis for short-term forecasts of precipitation from tropical systems making landfall (Visser *et al.,* 2004). The original technique, developed for GOES data by Spayd and Scofield (1984), has evolved into an automated tropical rainfall potential (TRaP) technique that combines SSM/I, advanced microwave sensor unit (AMSU), and TMI based estimates of rainfall with storm-track forecasts to produce forecasts of 24-hour precipitation prior to landfall (Ferraro *et al*., 2002).

Current PMW sensors used for estimation of rainfall include the Defence Meteorological Satellite Program (DMSP) SSM/I and the TRMM microwave imager (TMI). The SSM/I is a (near) polar-orbiting sensor aboard the DMSP platforms of the F-13, F-14, and F-15 satellites, and although there are usually two or three usable sensors at any one time resulting in a maximum of six overpasses per day, some regions receive only one overpass per day. The addition of the TMI sensor, in a low inclination orbit, only provides a modest increase in the daily coverage. Results from the series of precipitation intercomparison projects (PIP) (Adler *et al*., 2001) and the algorithm intercomparison programme (AIP) (Ebert *et al*., 1996) showed that the PMW algorithms are more accurate than the IR-based algorithms in terms of instantaneous rainfall estimates. However, the IR techniques provide better long-term estimates than the PMW techniques due to better temporal sampling: geostationary IR data nominally provides 48 samples each day (from Meteosat) compared with a maximum of 6 from the SSM/I sensors. Adler *et al*. (1993) noted that opportunities exist to improve precipitation estimates by combining the two types of data so that the strengths of individual algorithms are maintained rather than the weaknesses.

The IR data available globally every quarter hour is used as means to propagate PMW-derived precipitation features, producing spatially and temporally complete global precipitation analyses, (Joyce *et al*., 2004). These data provide good measurements of cloud-top properties; IR data is used to detect cloud systems and to determine their movement. The propagation of the cloud system is measured using, a method called cloud system advection vectors (CSAVs). This is an automated method that uses visible imagery. An interactive spatial lag correlation process is used to determine cloud system speed and direction as follows. At a given 5° latitude/longitude grid box that contains 8 km pixel resolution IR data at t = 0, a spatial correlation is performed among the IR pixel brightness temperatures in that grid box with those in the same domain but from

the t + 1/2 hour image. This process is repeated, but with each iteration, the spatial domain of the t + 1/2 hour grid box is shifted pixel by pixel in the zonal meridional directions. A primary domain is defined for each satellite, demarked by the midpoints between the nadir positions of primary and neighbouring satellites. Within each domain, CSAVs are derived solely from the primary satellite IR unless the daily image count falls below half of the overlapping neighbouring satellite daily image count; in this case, information from neighbouring satellite is used instead. When an image is missing for a particular half hour, vectors are determined by a linear temporal interpolation between the nearest past and future half-hourly vectors, weighted by the temporal distance from the missing time.

In case of microwave the propagation process of the PMW derived rainfall begins by spatially propagating initial fields of 8 km half-hourly instantaneous PMW analysis estimates (t + 0 hour) forward in time, by the discrete distance of the corresponding zonal and meridional vectors. Two auxiliary fields that are maintained along with each precipitation estimate are 1) time stamp (t = 0 for instantaneous), in which the column is propagated forward to produce analyses at t + 0.5 hour using IR-derived propagation vectors. This analysis is actually propagated one more time step to t + 1.5 hour, but in this case all values are overwritten by precipitation estimates from an updated PMW scan that became available at the t + 1.5 hour time step.

In addition to propagating rainfall estimates forward in time, a completely separate process is invoked in which instantaneous rainfall analyses are spatially propagated backward in time using the same propagation vectors used in the forward propagation, except for reversing the sign of those vectors.

2.2.3   Tropical Rainfall Measuring Mission

The tropical rainfall measuring mission (TRMM) is a joint National Aeronautical and Space Administration (NASA) and National Space Development Agency of Japan (NASDA) mission designed to measure tropical rainfall and its diurnal variability on a monthly time scale and in area of 10^5 km^2 (Visser *et al.,* 2004). TRMM was launched in 1998 and it orbits at an altitude of 350 km with a 35° inclination angle, which causes it to sample all local times every 23 days. Five instruments which measure various related aspects of precipitation are on board, namely:

(a) Precipitation radar (PR) – electronically scanning radar operating at 13.8-GHz; and spatial resolution of 4.3 km^2;

(b) TRMM microwave imager (TMI) – a nine channel radiometer that operates at five frequencies that are quite similar to the frequencies of SSM/I instrument, and makes measurements from 10 to 91-GHz. However, the TMI offers higher spatial resolution (4.6 x 6.9 km) than SSM/I (13 x 15 km) because of the relatively lower TRMM orbit (Joyce *et al.*, 2004),

(c) Visible and infrared scanner (VIRS) – a five channel imaging radiometer (0.63, 1.6, 3.75, 10.7, and 12.0 μm) with 2 km resolution;

(d) Lightning imaging sensor (LIS), and

(e) Clouds and earth's radiation energy system (CERES). Due to the lower orbit of the satellite, the resolutions of the sensor are much improved upon that of the SSM/I, resulting in a maximum resolution of 7 by 5 km at 85-GHz (Pan and Barnsley, 1999).

The precipitation weather radar provides three-dimensional structure of rainfall, particularly of the vertical distribution; quantitative rainfall measurements over land as well as over ocean and improvements in the overall TRMM precipitation retrieval accuracy by combined use of active (PR) and passive (TMI) and VIRS sensor data. The VIRS is a five-channel imaging spectral radiometer with bands in the wavelength range from 0.63 - 12 μm, and is similar to the advanced very high resolution radiometer (AVHRR) instrument (Visser *et al.*, 2004).

2.2.4 Combined Infrared and Passive Microwave techniques

Several forms of combined infrared and passive microwave techniques (IR – PMW) techniques have been developed to take advantage of the individual strengths of the IR and the PMW data. All of the available PMW data are converted to precipitation estimates on individual fields of view (FOVs), each dataset is averaged to the 0.25^o spatial grid over the time range ± 90 minutes from the nominal 3-hourly observation time (0000, 0300, …2100 UTC). The gridding is "forward'- each FOVs is averaged into the grid box(es) that contains its centre – except the AMSU-B gridding is "backward" – each FOV is approximately apportioned to the grid box(es) it occupies. All of these estimates are adjusted to a "best" estimate using probability matching of precipitation rate histograms assembled from coincident data (Huffman *et al.*, 2007).

One of the combined IR-PMW methods was developed by Adler *et al*. (1993) by modifying the GPI and the convective–stratiform technique (Adler and Negri, 1988) rain-rate values by comparing the IR results with that of an 85-GHz based algorithm over monthly timescales. This work has been extended to multisensor combined precipitation techniques currently used by the global precipitation climatology project (GPCP), which combine estimates by using weights based upon error estimates assigned to the individual components derived from monthly rainfall products. Kummerow and Giglio (1995) tested both fixed IR/variable rain-rate and variable IR/fixed rain-rate techniques over the Pacific atolls, again based upon monthly relationships. The universally adjusted GPI (UAGPI), described by Xu *et al*. (1999) used the scattering index (SI) of Ferraro and Marks (1995) to produce an optimal IR rain/no-rain threshold and optimal conditional rain rates in order to reduce the total error between the IR-based and the PMW based rainfall estimates. These techniques have a similar methodology: the adjustment of the IR product by the PMW product(s). Other methods use the PMW rainfall retrievals to calibrate against the IR temperatures so that the IR temperatures alone can be used to generate the rainfall.

Miller *et al*. (2001) developed a technique that generates rainfall from IR and PMW data using a linear brightness temperature (T_b) to rain-rate relationship. The common problem with the IR–PMW techniques has been the choice of the calibration domain. Many techniques, such as Adler *et al*. (1993) and Xu *et al*. (1999), use temporal domains spanning entire months to provide robust calibrations. However, while the monthly calibrations will reflect the climatological variations in the IR–PMW relationship they do not respond to the sub-monthly changes in the relationships. Instantaneous calibrations based upon coincident IR–PMW values have been utilized by Miller *et al*. (2001) and Turk *et al*. (2000), and have the advantage of responding to changes in the calibration over short-term periods.

Estimates from instruments based on GOES and polar operational environmental satellite (POES) possess a number of complementary strengths and weaknesses. Whereas VIS/IR-based estimates from GOES rely only on information from near the top of the cloud (i.e., cloud-top height, and in some cases microphysical information near the cloud top), microwave-based estimates from GOES are based on the concentration of water and ice throughout the cloud. However, these estimates are much

less frequent and have lower spatial resolution than the GOES data, making the GOES data necessary for analyzing heavy precipitation that occurs at relatively small scales in space and time.

A major problem facing the calibration of satellite estimates with validation data is the matching of the datasets both temporally and spatially. Errors noted by Kidd *et al.* (2003) include systematic errors due to satellite–ground misregistration that lead to a significant drop in statistical accuracy. Temporally coincident data are rarely achieved and several minutes leeway between the two datasets is often required. This can lead to displacement in position and changes in the spatial form of the precipitation. Finally, physical differences between satellite retrievals and validation retrievals exist and it is not realistic to assume that the satellite measurements will replicate those of the validation data precisely. These include resolution differences, viewing angles, and response to hydrometeors, and the characteristics of rainfall also need to be recognized (Joyce *et al.*, 2004).

In this way the observed frequency distribution of rain rates would be reflected in the resulting algorithm product. The technique can also be used to evaluate the relationship between two datasets where a regression line would not be meaningful. The premise of the cumulative histogram matching technique is that the measured rainfall is correct and that the satellite retrieval should produce a frequency distribution of rainfall rates similar to the microwave distribution over a certain region (Kidd *et al.*, 2003). Thus for a selected region the values of the satellite IR brightness temperatures and collocated measured rainfall (the PMW estimates) are accumulated into histograms that in turn is transformed into a cumulative histogram. These cumulative histograms are then matched so that the occurrence of heaviest measured rainfall is associated with the values of the satellite IR brightness temperature linked to be heaviest rainfall. The region over which the data is accumulated is primarily dependent upon the number of data points available: this need to be large enough for a reasonable sample size, but small enough to represent any local characteristics (Kidd *et al.,* 2003).

Note that the IR cumulative histogram is inverted since high temperatures are associated with no rain. The IR rain–no-rain threshold is the temperature with the same cumulative frequency as that of the PMW defined non-raining frequency. Increasingly colder IR temperatures are assigned increasingly higher rain rates so that the final distribution of

IR assigned rain rates is the same as that determined by the PMW data (Snijders, 1991). The technique therefore assumes a monotonically increasing rain-rate relationship with decreasing IR temperature with the premise that colder IR cloud-top temperatures are associated with higher rainfall than warmer clouds (Kidd *et al.*, 2003). The final relationship is that the rain–no-rain threshold is set at about 240 K, with temperatures of 220 and 210 K having rain rates of about 5 and 12.5 mm/h, respectively.

2.2.4.1   CMORPH technique

The Climate Prediction Centre morphing (CMORPH) is a technique developed at the National Oceanic and Atmospheric Administration (NOAA) Climate Prediction Centre (CPC). It is used to estimate global precipitation at very high spatial and temporal resolution by combining precipitation estimates derived from passive microwave observations exclusively, and uses spatial propagation information from geostationary data to propagate passive microwave features (Joyce *et al.*, 2004). At a given location, the shape and intensity of the precipitation features in the intervening half hour periods between microwave scans are determined by performing a time-weighting interpolation between microwave-derived features that have been propagated forward in time from the previous microwave observation and those that have been propagated backward in time from the following microwave scan. This latter step is referred as "morphing" of the features.

The propagation process is illustrated graphically in Figure 2.2. An initial 0330 GMT time analysis of instantaneous PMW rainfall (t = 0 hours) consisting of two clusters over a region in South Pacific (Fig. 2.2a, leftmost) is propagated forward to produce analyses at t + 0.5 and t + 1 hour (Fig. 2.2a) using IR-derived propagation vectors. This analysis is actually propagated one more time step to t + 1.5 hour, but in this case all values are overwritten by precipitation estimates from an updated PMW scan (Fig. 2.2a, rightmost column) that became available at the t + 1.5 hour time step (0500 GMT). The continuity of the propagated rainfall clusters in the t + 0.5 and t + 1.0 hour fields can be appreciated by comparing them with the updated PMW analysis (Fig. 2.2a, rightmost column), although in this case, the propagation rate appears to be slightly slow.
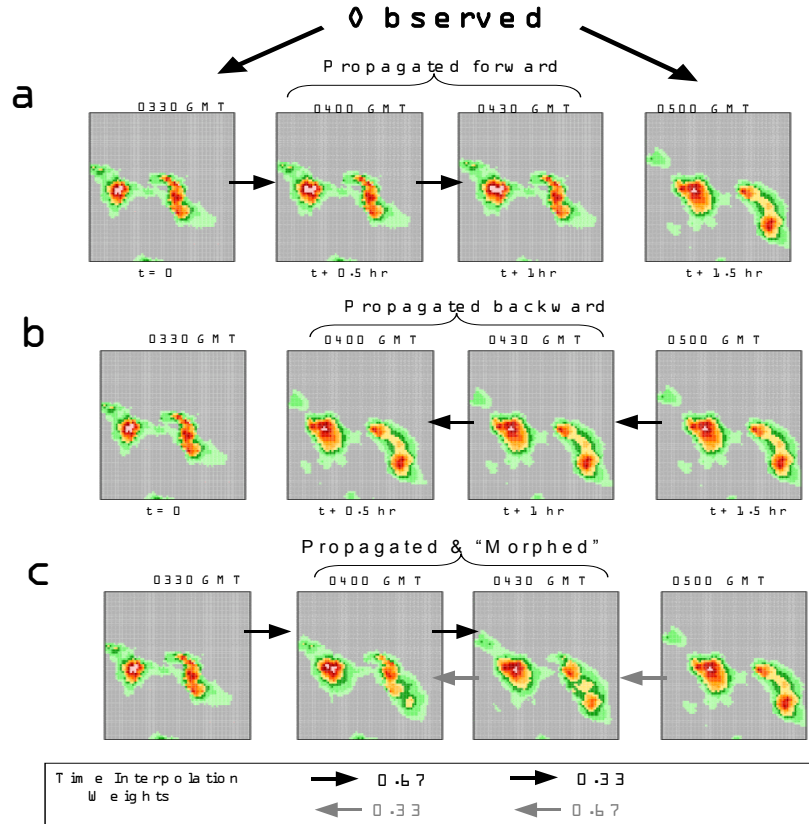
Figure 2.2: Description of the propagation and morphing process for a region in the South Pacific (Source: Joyce *et al.*, 2004)

In addition to propagating rainfall estimates forward in time, a completely separate process is invoked in which instantaneous rainfall analysis are spatially propagated backward in time using the same propagation vectors used in the forward propagation, except for reversing the sign of those vectors. The results are stored separately from those computed in the forward propagation process. Thus for the above example, $t = 1.5$ hours updated observed PMW precipitation (Fig. 2.2b, rightmost column) is propagated backward to the $t = 0$ hour time frame (Fig. 2.2b, leftmost column). When all propagated fields have been computed, the $t = 0$ hour analysis that contains observed data overwrites the propagated estimates for that time stamp. The backward propagation procedure begins at least 5 hours beyond the initial analysis time in order to have a nearly globally complete field of backward-propagated rainfall estimates due to the temporal sampling considerations imposed by the orbital nature of the spacecraft (Joyce *et al.*, 2004). This constraint delays the operational availability of CMORPH by 5 hours

previous to the most current half hour of combined PMW rainfall input analysis. However, by propagating the rainfall analysis temporally in both directions, the propagation speed and direction is improved over doing this in a single direction only. To this point, only the propagation of PMW derived rainfall patterns, when and where PMW data are not available, has been shown. However, a simple propagation of the features themselves will not change the character of those features but will merely translate them to new positions. Changes in the intensity and shape of the rainfall features are accomplished by inversely weighting both forward and backward.

Although the precipitation estimates are available on a grid with a spatial resolution of 8 km (at the equator), the resolution of the individual satellite derived estimates is coarser typically 12 x 15 km.

The PMW derived precipitation estimates that are presently used in CMORPH are generated from observations obtained from the NOAA polar-orbiting operational meteorological satellites, the DMSP, and from TRMM satellites (Kummerow and Giglio, 1995). The PMW instruments aboard these satellites are the AMSU-B, the SSM/I, and the TMI, respectively.

Rainfall estimates derived from the TMI and SSM/I instruments are in very good agreement as is expected since the two sensors are quite similar in design, and the differences that do exist between them are attributed largely to the different retrieval footprint resolutions because they are flown at different altitudes. However, rainfall derived from the AMSU-B algorithm differs in many respects from SSM/I and TMI rainfall techniques (Joyce *et al*., 2004). The algorithms that are applied to these data generate precipitation estimates using similar channels, because the SSM/I and TMI instruments are equipped with channels that detect both emission and scattering signatures.

The strengths of the CMORPH algorithm is that the inaccuracies of the use of IR data for rainfall estimation are eliminated through the sole use of passive microwave retrievals for rainfall derivation. Both forward and backward in time spatial propagation of PMW rainfall extends the use of relatively accurate, however, instantaneous PMW estimation into spatially and temporally complete precipitation analyses. CMORPH

adequately propagates rainfall that moves relatively in synchronous with associated high elevation cloud cover.

The CMORPH is related to the following weaknesses: Rainfall that develops, matures, and decays (i.e. especially warm season afternoon convective complexes over land) between all available satellites PMW swaths will obviously not be detected by the PMW estimated rainfall used as input into CMORPH. Rainfall that does not move in synchronous with associated high elevation cloud cover will not benefit from the IR derived propagation of CMORPH. An example of this would be the common horizontal wind shear found in South America resulting from a persistent upper level anti-cyclone, west of the continent, equator-ward pushing cirrus that emanating from rainfall complexes often propagating southward (Joyce *et al., 2004)*.

2.2.4.2   *NRL blended technique*

The Naval Research Laboratory blended (NRLB) satellite technique is based upon area-dependent statistical relationships derived from a precise, near real-time ensemble of collocated passive microwave (PMW) and infrared (IR) pixels from any or all low earth-orbiting (LEO) and geostationary satellites (Turk *et al.*, 2003), respectively, as their individual orbits and sensor scan patterns continuously intersect in space and observation time.

Near real-time digital datasets are maintained on an anonymous file transfer protocol (ftp) site, in a simple-to-read binary rectangular map projection. The technique is developed to work at a very basic level and then can work with additional capabilities depending upon which satellite datasets, channels, and ancillary data are available. This technique requires (at a minimum) the basic 11 µm longwave IR window channel. The spatial resolution is 0.1^{o} finest scale. The maximum time scale is any multiple of 3 hour (6, 12, 24, 48, etc). Temporal scale instantaneous, but 3-hourly accumulations are the shortest time-interval accumulation.

2.2.4.3.   *PERSIANN technique*

The Precipitation Estimation from Remotely sensed information using artificial neural networks (PERSIANN) is an IR and PMW merged estimation method that uses neural

network function procedures to estimate 15 min rainfall rates at 0.25° x 0.25° spatial resolution using infrared brightness temperature images provided by geostationary satellites (GOES – 8/9/10, GMS - 5, and Meteosat-8), and TRMM TMI instantaneous rain from NASA, and a previously calibrated neural network mapping function. The system classifies satellite images according to cloud-top IR brightness temperature and texture at around the estimation pixel (Sorooshian, *et al*., 2000). The PERSIANN system rainfall product covers 50°S to 50°N globally, (Janowiak *et al.,* 2000). The estimated PERSIANN 30-minute rain rates are aggregated to 6-hour accumulated.

2.2.4.4. *Multiple Precipitation Analysis technique*

The Multiple Precipitation Analysis (MPA) algorithm is a combination of merged TRMM high quality (HQ) microwave estimates and the variable rain rate (VAR) IR estimates that are rescaled to monthly data (Huffman, *et al*., 2003). It produces gridded estimates on a 3-hour temporal resolution and 0.25^o spatial resolution in a global belt extending from 50° S to 50° N latitude (Huffman *et al*., 2001). The MPA estimates are produced in four stages:

- (a) the microwave precipitation estimates are calibrated and combined,
- (b) infrared precipitation estimates are created using the calibrated microwave precipitation,
- (c) the microwave and IR estimates are combined, and
- (d) rescaling to monthly data is applied.

(a) Microwave precipitation estimates

The passive microwave data available are converted to precipitation estimates to be used, then each dataset is averaged to the 0.25^o spatial grid over the time range 90 minutes from the nominal observation time. All of these estimates are adjusted to a best estimate (Huffman *et al*., 2001) using probability matching of precipitation rate histograms assembled from coincident data.

(b) Infrared precipitation estimates

The MPA uses two different IR datasets for creating the complete record of 3-hourly 0.25^o gridded base temperatures. Histograms of time-space matched HQ precipitation rates and IR brightness temperatures, each represented on the same 3-hourly 0.25^o grid, are accumulated for a month, and then used to create spatially varying calibration

coefficients that convert IR brightness temperatures to precipitation rates. After calculation of the HQ-IR calibration coefficients, these are applied to each 3-hourly IR dataset during the month (Huffman *et al.*, 2001).

(c) Combined microwave and infrared precipitation estimates

In this stage, a "best" estimate of precipitation is provided in each grid box at each observation time. The process of combining passive microwave estimates is relatively well-behaved because the sensors are quite similar and is used for most retrievals. For combining the HQ and VAR estimates, the physically-based HQ estimates are taken "as is" where available and the remaining grid boxes are filled with VAR estimates. According to Huffman *et al.* (2001), this scheme provides the "best" local estimates, at the expense of a time series that is from datasets displaying heterogeneous statistics.

(d) Rescaling to monthly data

The final step in generating MPA is the indirect use of rain gauge data. All available 3-hourly HQ + VAR estimates are summed over a calendar month to create a monthly multi-satellite product.

2.3 Comment

Monitoring rainfall from satellite imagery is an attractive alternative as it has the potential for good spatial coverage, is available in near real time and is relatively inexpensive to access. Most of algorithms for satellite-based rainfall monitoring rely on simple empirical algorithms that make use of geostationary thermal infrared data, sometimes by combining the passive microwave imagery from polar-orbiting satellites or rain gauge data available via Global Telecommunications System (GTS).

The combined infrared and passive microwave estimates provides good spatial and temporal resolution. In this study, four methods that combine infrared and passive microwave data were selected. These are CMORPH, MPA, NRLB and PERSIANN. The methods were selected because of availability of satellite data and ease of comparison between the methods in different regions of the world.

Chapter 3   DATA and METHODS

3.0   Introduction

Mozambique has three main river basins namely the Limpopo, Save and Zambezi
basins. All these basins are prone to weather extremes such as droughts and floods. It is
therefore necessary to investigate the effects of rainfall variability on the hydrology of
the river basins. Heavy rains in northern South Africa, southern Botswana and
Zimbabwe flow directly into the Limpopo basin causing floods. Floods produce a major
negative impact on the region's macro-economic performance, the environment and
people's welfare which is why individual governments are attempting to mitigate and
manage this threat. Despite these efforts, planning for floods remains inadequate leading
to loss of human and animal life. This is the reason why this area was selected for this
study.

To estimate areal rainfall over the Limpopo basin using satellite data, four algorithms
that combine infrared and passive microwave data, namely, Climate Prediction Centre
morphing (CMORPH), the precipitation estimation from remotely sensed information
using artificial neural networks (PERSIANN), the multiple precipitation analysis
(MPA), and the Naval Research Laboratory blended (NRLB) were used.

The following sections describe the characteristics of the study area, source of satellite
and gauge data, and the validation procedures applied in this study.

3.1   Description of the Study Area

The Limpopo Basin (Figure 3.1) is almost circular in shape with a mean altitude ranging
from 0 - 1000 m above sea level. It lies between latitudes 20°S - 25°S and longitudes
25°E - 35°E. The total surface area drained by the basin is estimated at about 412 938
km^2. Of the basin's total area, about 44 percent is occupied by South Africa, 21 percent
by Mozambique, almost 19 percent by Botswana and 16 percent by Zimbabwe (Boroto,
2000).
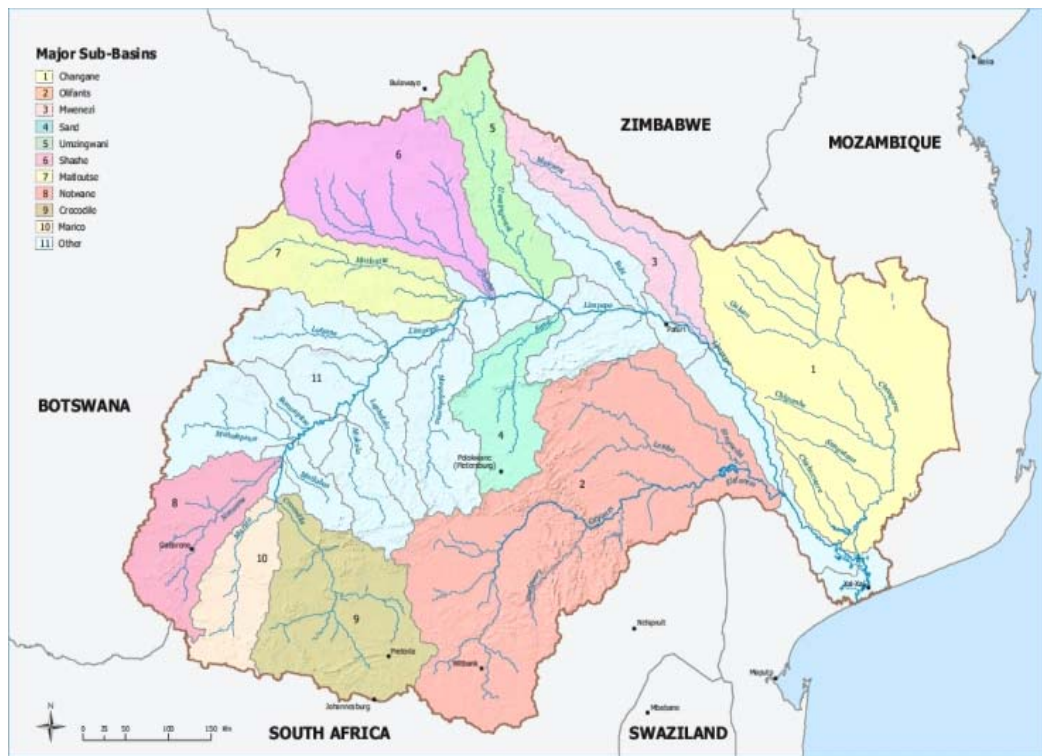
Figure 3.1: Map of study area showing the Limpopo Basin and the riparian countries
(Source: Atlas for Disaster Preparedness and Response in the Limpopo Basin, 2003)

The Limpopo River has a relatively dense network of more than 20 tributaries, though most of these tributaries have either seasonal or episodic flows. In historical times, the Limpopo was a strong-flowing perennial river but is now regarded as a weak perennial river where flows frequently cease. According to FAO (2001), during drought periods, no surface water is present over large stretches of the middle and lower reaches of the river.

The Elefantes (or Olifants in South Africa) part of the lower Limpopo section, has the largest river catchment area. The Elefantes and its major tributaries bring the most water to the Limpopo. Figure 3.2 shows the course of the Limpopo river and its major tributary, the Elephantes.
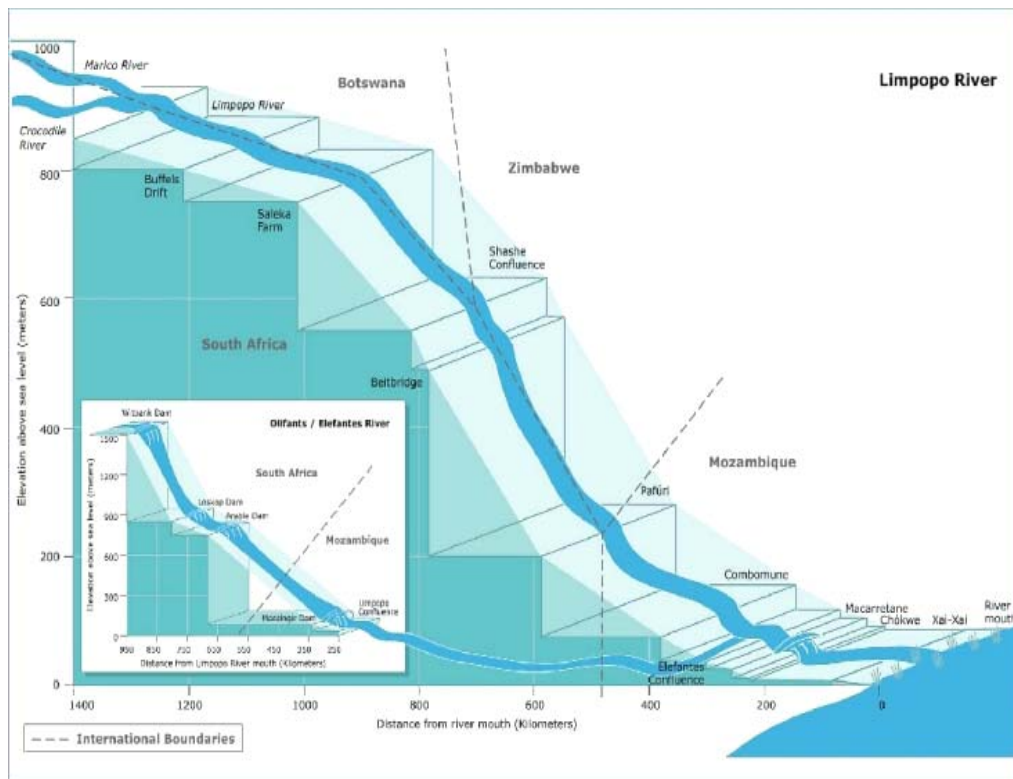
Figure 3.2: Course of the Limpopo River and its major tributary, the Elefantes/Olifants (Source: Atlas for Disaster Preparedness and Response in the Limpopo Basin, 2003)

The basin consists largely of undulating terrain between ranges of hills and mountains. The northward flowing (South African) tributaries of the Limpopo river have incised deep gorges through the hills and mountain ranges that are visible as erosional remnants. Elsewhere, the river valleys are broad and flat-bottomed with river channels that are slightly or moderately incised into the surrounding parent material (Schulze, 1997).

The upstream portion of the Limpopo is characteristically flat with kopjes and small hills rising not more than 200 m above the general level and occasional elongated ridges of more resistant strata forming the only local relief. The relief is more pronounced in the south-eastern corner where the quartzites of the Transvaal Sequence, which form the ridges of the Magaliesberg and the Witwatersrand, have been deeply incised by the river to depths of up to 600m. The Waterberg Plateau forms another area of more pronounced relief on the eastern side of the central portion of the basin (FAO, 2001).

Large portions of the central and western parts of the Limpopo Basin (especially in the Shingwedzi and Letaba sub-catchments) have very little or poor drainage, and are

33

usually considered to be endorheic (internally draining). These areas are often marked by the formation of saltpans or clay-bottomed pans where rainfall collects and evaporates. These areas are generally subjected to mechanical (physical) weathering processes, in contrast to the predominance of chemical weathering processes in the wetter headwater regions of most tributaries. The Mozambique portion of the Limpopo basin consists of gently undulating terrain with numerous small tributary streams and pools forming part of the Changane drainage system. This tributary rises close to the Zimbabwe - Mozambique border, meanders across the Mozambique coastal plain and joins the Limpopo River very close to its mouth on the coast near the town of Xai-Xai. A belt of heavy textured soils connecting the Limpopo and Incomati river systems suggests that the Limpopo previously also entered the Indian Ocean via Maputo Bay (Atlas for Disaster Preparedness and Response in the Limpopo Basin, 2003).

The dominant soil types of the basin are moderately deep sandy to sandy-clay loams in the south, grading to shallower sandy soils in the north and deeper sandy soils in the west and east. There are few extensive areas of black vertisols in the southern parts of the basin. Deep layers of wind-blown Kalahari sands cover large areas of the western portion of the Limpopo Basin, while the sandy soils of the eastern (Mozambique) portion are derived from old, unconsolidated marine sands. The valley bottom soils along all of the tributary rivers and the Limpopo main channels are generally of colluvial or alluvial origin (Mafoko, 1990 and Dennett, 1987).

The Limpopo River Basin is a characterized by summer rainfall, generally with low precipitation. The overall feature of the mean annual precipitation is that it decreases fairly uniformly westwards from the northern reaches of the Drakensberg Escarpment across the interior plateau, however, rainfall is highest on the Drakensberg Escarpment because of its orographic effect (Schulze, 1997). There is also a north-south gradient towards the Limpopo River. Rainfall varies from a low of 200 mm in the hot dry areas to 1500 mm in the high rainfall areas. The majority of the catchment receives less than 500 mm of rainfall per year. The hot dry areas receiving about 200 – 400 mm of annual rainfall are located mostly within the main Limpopo River Valley itself. The severe droughts observed during the early 1990s and the recent exceptional floods in the Limpopo valley in 2000 illustrate the extreme variability of rainfall and runoff in the basin.

Three wind systems have been identified as having a strong influence on the basin's climate. These are the tropical cyclones from the Indian Ocean; the southeasterly wind systems that bring rainfalls from the Indian Ocean; and the inter-tropical convergence zone (ITCZ), which in some years moves sufficiently far southwards to influence rainfalls in the northern parts of the basin (Lindesay, 1998).

Air temperatures across the basin show a marked seasonal cycle, with highest temperatures recorded during the early summer months and lowest temperatures during the cool, dry winter months. In summer, daytime temperatures may exceed 40º C, while in winter temperatures may fall to below 0º C. The air temperatures are closely related to altitude, and also to proximity to the ocean. The mean maximum temperature in most of the Limpopo basin, notably South Africa, Botswana and Zimbabwe, varies from about 30 - 34º C in the summer to 22 - 26º C in winter. The mean minimum daily temperature in most areas lies between 18 - 22º C in summer and 5 - 10º C in winter (Atlas for Disaster Preparedness and Response in the Limpopo Basin, 2003).

3.2 Source of Satellite Data

In this study the four algorithms (CMORPH, MPA, NRLB and PERSIANN) used two main satellite datasets, namely visible (VIS)/infrared (IR) and passive microwave data. The VIS/ IR data were collected from the geostationary operational environmental satellite (GOES) and from European organization for the exploitation of meteorological satellites (EUMETSAT). These are GOES-9 at 155 E, GOES-10 at 135 W, GOES-12 at75 W, and Meteosat second generation (MSG) at 5E. The GOES satellites use the visible and infrared spin scan radiometer (VISSR) sensor. The MSG covers a global region between 60° S and 60° N. The IR data on MSG was measured by radiometer called spinning enhanced visible and infrared imager (SEVIRI) in the IR10.8 μm channel. In this channel, the instrument measures earth surface, cloud top temperatures, wind fields and atmospheric instability (EUMETSAT, 1998). Detection of cirrus and inference of total precipitable water vapour over sea is also provided by the sensor in the IR13.4 μm channel. The IR data is at temporal and spatial resolution of 15 minutes and 3 km respectively.

National Oceanic and Atmospheric Administration (NOAA), Defence Meteorological Satellite programme (DMSP) and from Earth-orbiting system (EOS) Aqua satellites.

The passive microwave (PMW) satellite-based rainfall algorithms which derive precipitation utilize data from low-earth orbiting satellite sensors, which sample wide swaths of Earth in either a conical or across-track scan pattern. The current operational constellation includes the Tropical rainfall measuring mission (TRMM) microwave imager (TMI) and its companion precipitation radar (PR), three advanced microwave sounding units (AMSU-B) onboard NOAA-15/16/17, the advanced microwave scanning radiometer (AMSR-E), onboard EOS-Aqua, three special sensor microwave imager (SSM/I); on board DMSP F-13/14/15. The AMSU-B measures atmospheric emissions in the 50 to 60-GHz range for profiling the temperature of clouds (Rao *et al.,* 1990), and the SSM/I is seven channel linearly polarized PMW radiometer operating at four frequencies, namely 19.35, 22.235, 37.0 and 85.5-GHz. Table 3.1 shows the characteristics of the satellites and the data required for each algorithm.

Table 3.1: Characteristics of satellites and data required for the algorithms

Satellite	Type of data	Sensor	Algorithms
Meteosat - 8 (MSG)	IR	SEVIRI	CMORPH, MPA, NRLB and PERSIANN
GOES-9, 10, 12	IR	VISSR	CMORPH, MPA, NRLB and PERSIANN
NOAA (15, 16, 17,)	PMW	AMSU-B	CMORPH, MPA, NRLB and PERSIANN
DMSP (13, 14, 15)	PMW	SSMI	CMORPH and MPA
TRMM	PMW	TMI	CMORPH, MPA and PERSIANN
Aqua	PMW	AMSR-E	CMORPH and MPA

3.2.1   *Algorithm processing*

The combined infrared and passive microwave rainfall algorithms (CMORPH, MPA, NRLB and PERSIANN) use three key stages to process the datasets:

> (i)   dataset generation,
>
> (ii)   calibration, and
>
> (iii)   application.

(i)   Dataset generation

- Rainfall estimates from the PMW are remapped to a 0.1^o grid for each 30 minute period centred on the hour and half-hour.

- IR derived rainfall data are subsampled to a 0.1^o grid by using a 3 x 3 mean filter to average the 4 km data and generate a mean cloud-top temperature over 12 km x 12 km area. This approximates the maximum resolution of the PMW rainfall estimates.

- Each collocated PMW and IR pixel for each 30 minutes (±15 minutes) and 0.1^o x 0.1^o area is entered into a database that records histograms of IR temperatures (75 - 329 k) and PMW rainfall estimates (0.0 – 51.1 mm/h). All data-present regions of the database are then saved onto disk for later use.

(ii)   Calibration procedure

The calibration procedure requires that sufficient data be used to ensure a stable relationship between the IR and PMW datasets. The current techniques carry out a calibration procedure once per day using a temporally and spatially weighted aggregation of the data from the database. The operational scenario uses data for d_o (current day) back to d_{-4} (day minus four) and is accumulated using an arbitrarily derived linear weighting function (i.e., d_o has a weight of 1, $d_{-1} = 0.8$, $d_{-2} = 0.6$, etc.).

After the data has been aggregated temporarily it is then smoothed spatially through the use of a 5° x 5° Gaussian filter. Thus separate histograms of collocated IR temperatures and PMW rainfall rates are generated. These are converted into cumulative histograms and are then matched through the use of a cumulative histogram matching approach so that the coldest IR temperatures are assigned the highest rainfall. These relationships for each 0.1^o x 0.1^o area are saved as a lookup table that enables efficient processing of subsequent calculations.

(iii) Application

Each 30 min image is then processed using the current calibration at the subsampled IR resolution of 12 km to generate rainfall.

3.2.2 Satellite product development

This section describes the development of satellite product by CMORPH algorithm. The CMORPH satellite-based rainfall estimation is developed in two levels:

(i) Product development level 1

The CMORPH algorithm develops 30 minute, 8-km matrices of all PMW sensors combined rainfall, and calibrates to TRMM TMI. After this stage it maps all PMW rainfall into rectilinear 0.0727 latitude/longitude resolution (8-km at equator), 30 minute arrays for each sensor-type/algorithm. Then calibration of each sensor-type/algorithm rainfall to TMI is done by using frequency matching, heaviest to lightest rain rates, and separates for 10 degree latitude bands, and surface type.

By using PMW from AMSU-B, propagation vector matrices are developed every 30 minutes at 2.5^{o} resolution then is created the cloud system advection vector (CSAV) arrays from spatial lag correlation of successive 30 minute merged IR also using the 2.5^{o} resolution. The PMW rainfall propagation vector matrices are produced by tuning CSAV to spatially and temporally matched radar rainfall propagation.

(ii) Product development level 2

The propagation and morphing of PMW precipitation is done as follows:
Spatially propagate, forward in time, 8 - km combined PMW rainfall from "past" orbits using rainfall propagation matrices. In a separate processing, spatially propagate, backward in time, 8- km combined PMW rainfall from "future" orbits using rainfall propagation matrices. Then morph rainfall by inversely weighting both forward and backward propagated rainfall by the respective temporal distance from observed PMW precipitation. The output is a 30 minute 0.0727 latitude/longitude (8 km at equator) CMORPH.

3.3 Source of Rainfall Data

The rainfall data used in this study was measured using rain gauges in the Limpopo basin. The data was obtained from the National Institute of Meteorology of Mozambique (12 rain gauges), South African Weather Service (70 rain gauges),

Meteorological Service of Botswana (5 rain gauges), and from Meteorological Services Department of Zimbabwe (3 rain gauges), for the period 1 October 2005 - 31 March 2006. The study period was selected taking into account the availability of satellite data for the study area.

3.4 Validation

The time scale of primary interest to this study is daily rainfall validation, largely because the bulk of the rain gauge observations available for use in algorithms validation are 24 hour accumulations. Four satellite rainfall algorithms (CMORPH, MPA, NRLB and PERSIANN) producing 24 hours accumulated rainfall estimates on daily basis in near-real time were evaluated. The satellite rainfall estimates were validated using rain gauge data over the Limpopo Basin for the rainfall season corresponding to the period 1 October 2005 to 31 March 2006. Very little rainfall was recorded over the basin during the season, as shown in Figure 3.3. The months of January and February 2006 recorded an average rainfall of about 55 mm/month. The total area average rainfall observed in the area was 195 mm, less than the average rainfall that is normally observed in the region.
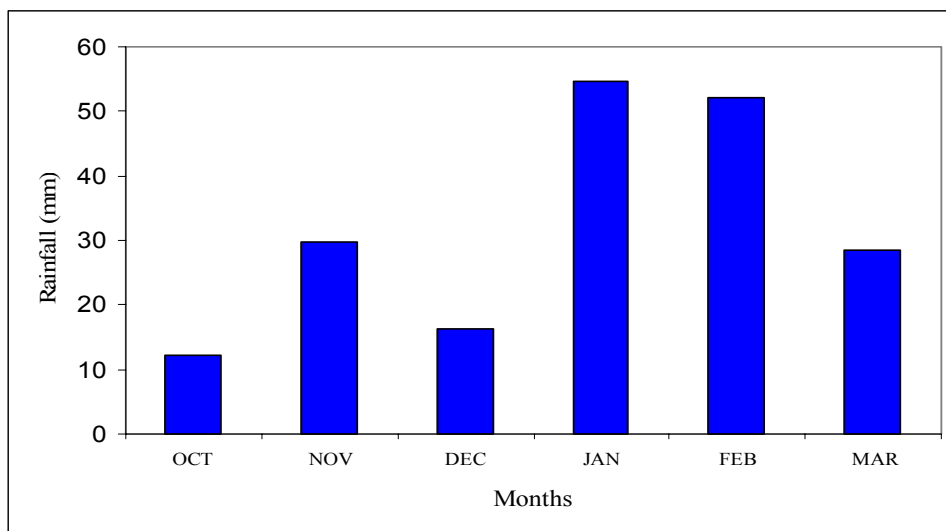

Figure 3.3: Monthly average rain gauge in the Limpopo Basin during 2005/2006 rainfall season (for 90 rain gauges)

The rainfall data was averaged into grid boxes of 0.25^o x 0.25^o, using the inverse-weighting interpolation method. The satellite estimates were developed also using 0.25^o resolution. A surface mask was used over the Limpopo Basin. Figure 3.4 shows the flow of rain gauge and satellite data for validation process.

```
┌──────────────────────┐          ┌──────────────────────┐
│   Daily rain gauges  │          │    Global satellite  │
│        from          │          │ quantitative         │
│  Botswana, Mozambique,│         │ precipitation        │
│  South Africa and    │          │    estimation        │
│     Zimbabwe         │          │       at             │
│                      │          │  0.25 degree grid    │
└──────────────────────┘          └──────────────────────┘
          │                                    │
          ▼                                    ▼
┌──────────────┐   ┌────────────┐   ┌──────────────────┐
│   Extract    │   │  Generate  │   │     Extract       │
│   gauges     │◄──│0.25 degree │──►│  quantitative     │
│   over       │   │   grid     │   │  precipitation    │
│Limpopo Basin │   │   over     │   │  estimation       │
│              │   │Limpopo     │   │     over          │
│              │   │  Basin     │   │  Limpopo Basin    │
└──────────────┘   └────────────┘   └──────────────────┘
       │                                     │
       │          ┌──────────────┐           │
       └─────────►│  Validation  │◄──────────┘
                  │ results for  │
                  │ the Limpopo  │
                  │    Basin     │
                  └──────────────┘
        ┌──────────────┐      ┌──────────────┐
        │ Maps of gauge│◄──┐  │  Validation  │
        │analysis and  │   │  │ Statistics   │
        │satellite     │   └─►│ for the      │
        │products for  │      │Limpopo Basin │
        │the Limpopo   │      │              │
        │   Basin      │      │              │
        └──────────────┘      └──────────────┘
```
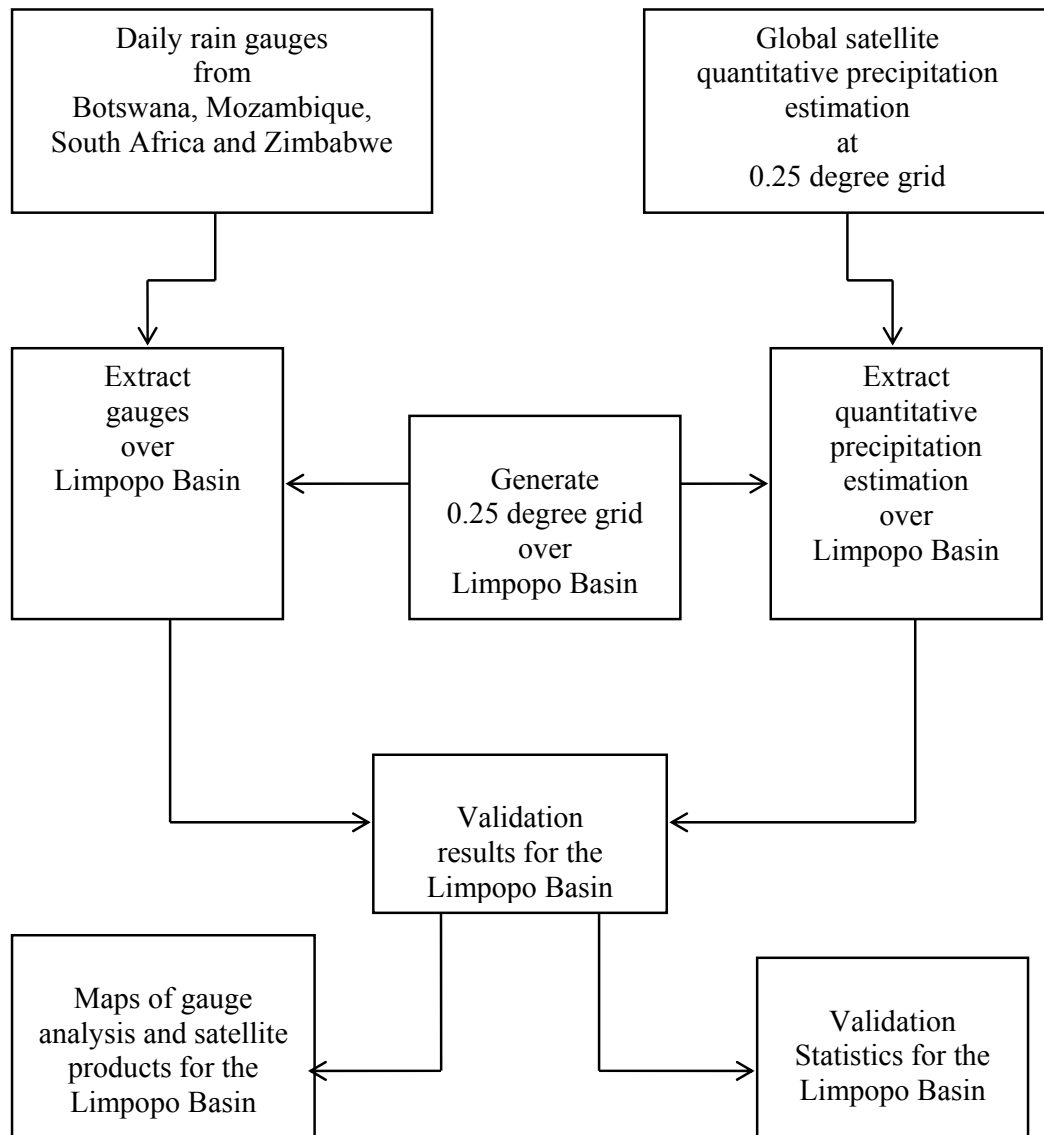
Figure 3.4: Overview of data flow in validation process.

A variety of validation approaches were used to measure different aspects of algorithm quality. To measure skill for rain occurrence, continuous statistics such as frequency bias are evaluated. The bias indicates whether the estimation system has a tendency to

underestimate (bias < 1) or overestimate (bias > 1) events. This is the measure of relative frequencies.

In order to measure the fraction of observed events that were correctly estimated, probability of detection (POD) was calculated. The POD represents how often real precipitation events are detected by the techniques. It ranges from zero (no detection) to one (perfect detection). Also in the same range (0-1) is the false alarm ratio (FAR) which represents how often false precipitation events are registered (given no actual event). To measure the fraction of observed and/or estimated events that were correctly estimated, equitable threat score (ETS) was calculated. The perfect score is 1 and ETS ranges from -1/3 to 1. Zero indicates no skill. The Hanseen & Kuipers score (HKS) or true skill statistic was calculated to indicated the ability of the estimation to separate the "yes' cases from the "no" cases, and it ranges from -1 to 1. In addition, to get more representative idea of real accuracy (Ebert *et al.*, 1996) both in situations where rare events are involved and in situations where climatological frequencies of the categories are nearly equal, the critical success index (CSI) was calculated. It evaluates the fraction of observed and/or estimation rainfall that were correctly estimated, and ranges from 0 to 1. To quantify errors in rain amount, the mean absolute error, the root-mean square error (RMSE), and the correlation coefficient were calculated. The several of the statistics used in this study were calculated from 2 x 2 contingency table in which 1 mm/day is the threshold for rain versus non rain occurrence (Table 3.2). The definitions of these statistical parameters are presented in Appendix I.

Table 3.2: Contingency table for categorical statistics used in the study

Event observed		Event estimated		Total observed
		Yes	No	Total observed
	Yes	h (hits)	f (false alarm)	h + f
	No	m (misses)	z (correct negative)	m + z
	Total estimated	h+m	f+z	h + f + m + z

(Source**:** after Stephenson, 2002)

Here: hits (h) represents observed rain correctly detected, miss (m) is observed rain not detected, false alarm (f) is rain detected but not observed, and correct negative or null event (z) means no rain observed nor detected.

3.5   Software used for "data processing"

The processing of rain gauge data was done using interactive data language (IDL) software. For this study the IDL was LINUX based software and provides maps and some statistical tests. This software was developed at the University of Minnesota in the USA (www msi.umn.edu).

Chapter 4   RESULTS and DISCUSSION

4.0   Introduction

Rain gauge data is the only ground-based data available for validating the satellite -
based rainfall estimation over the majority of Southern Africa. Unfortunately rain
gauges are not without error themselves when measuring precipitation due to the
interactions of the gauge and their microenvironment (Layberry *et al*., 2006).
Additionally, as mentioned above, gauge data over much of the subcontinent are
sparsely distributed.

Flitcroft *et al*. (1989) analysed data from a dense rain gauge network in West Africa and
showed that the standard deviation of individual point values used to represent a given
pixel (10 x 10 km) average rainfall was approximately 10 mm and this value was almost
independent of rainfall quantity. They also found a systematic bias in that gauge
measurements of high rainfall amounts were likely to overestimate the pixel average
rain. It is reasonable to suppose that convective rainfall associated with the ITCZ
elsewhere in Africa would display similar variability.

This chapter presents the study outputs in the form of maps for the daily area average
satellite estimates and observed rainfall, tables and graphs for analysis of the statistical
parameters, and the chapter includes the main constraints found during the analysis of
the results.

4.1   Results

The variability of the results of satellites estimates and gauge data at daily basis is
analysed and discussed in this section. Both satellite estimates and gauge rainfall
correspond to the daily area average for the Limpopo basin during 2005/2006 rainfall
season.

4.1.1 *Comparison of satellite rainfall estimation with rain gauge data*

The multi-algorithm map is a quick-look display of the rain gauge analysis and all of the satellite-based rainfall estimates. This display enables an easy comparison of different products, by using the "eyeball" or visual method. Figure 4.1 shows a comparison between the CMORPH algorithm and gauge daily area average rainfall for 25 February 2006 over the Limpopo basin which represents one of the best results at daily basis for the study period. The validation results for MPA, NRLB, and PERSIANN methods for the same day are given in Figures 4.2, 4.3 and 4.4, respectively.

A scatter plot (lower left) shows the direct correspondence between the estimates and the analysed rain amounts. The occurrence of precipitation for matched observed: estimated values are shown in the lower left. Ideally the portions of colour within each of the estimated and observed bars should be equal but in this case the CMORPH algorithm estimate overestimates the rainfall.

The accumulation of precipitation by intensity is shown immediately below the occurrence bars. The bar length is normalized by the maximum of the estimated and observed total. This provides information on the contribution of precipitation intensities to the precipitation total. On the centre bottom is the descriptive statistics, with contingency table, and finally, the basic set of statistics is provided in the lower right.
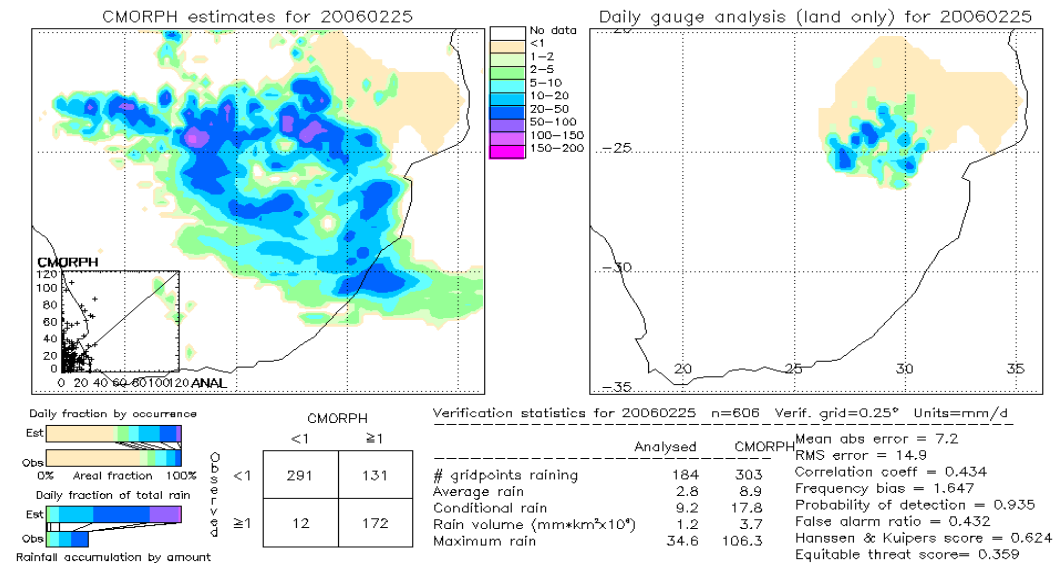
Figure 4.1: Validation of CMORPH algorithm for 25 February 2006 over the Limpopo Basin
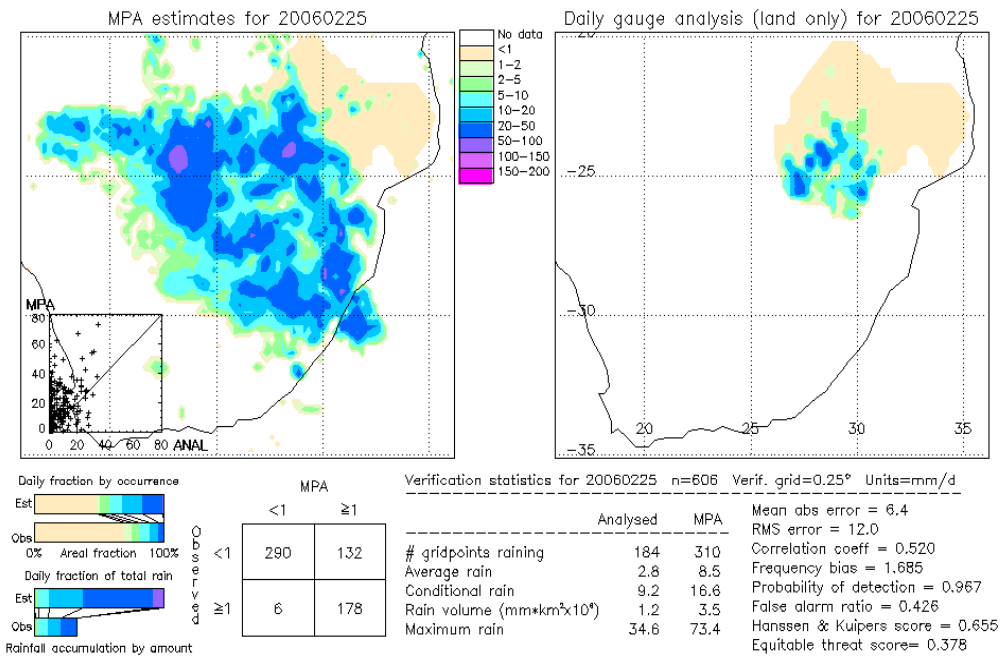
Figure 4.2: Validation of MPA algorithm for 25 February 2006 over the Limpopo Basin
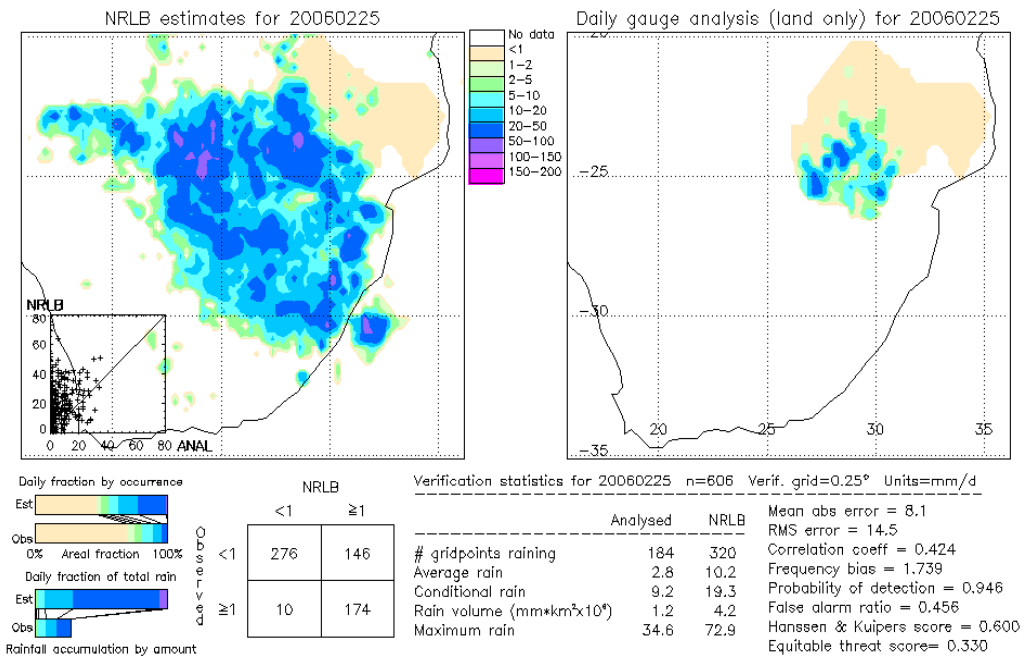

Figure 4.3: Validation of NRLB algorithm for 25 February 2006 over the Limpopo Basin
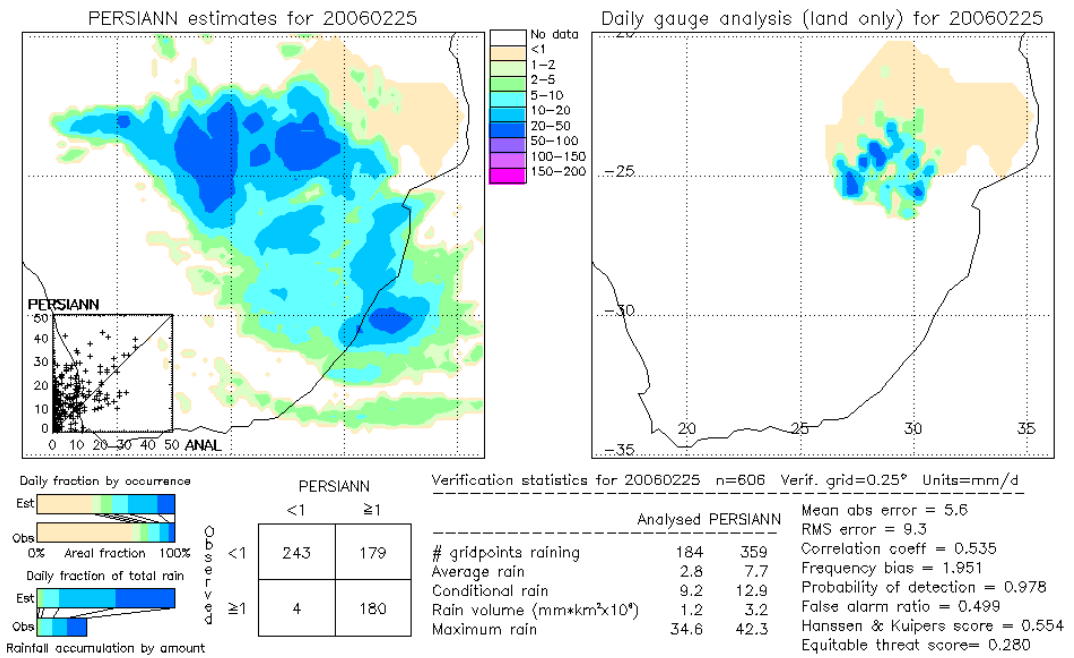
Figure 4.4: Validation of PERSIANN algorithm for 25 February 2006 over the Limpopo Basin

During 25 February 2006, all four satellite algorithms overestimated rainfall in the Limpopo Basin. The values of positives bias ranged from 1.1 – 1.9 and the root-mean square errors was at range between 9.3 – 14.9. The values of probability of detection (POD) and false alarm ratio (FAR) showed that the algorithms were good in detecting rainfall and it is also demonstrated by the Hanssen and Kuipers score (HKS) and the Equitable Threat score (ETS).The HKS and ETS ranged between 0.55 – 0.65 and 0.28 – 0.38, respectively. Table 4.1 shows the summary of the statistical parameters for 25 February 2006.

Table 4.1: Summary of some statistical parameters for 25 February 2006

Algorithms	Root-mean square error	Bias	POD	FAR	HKS	ETS
CMORPH	14.9	1.6	0.90	0.43	0.62	0.36
MPA	12.0	1.1	0.97	0.43	0.65	0.38
NRLB	14.5	1.7	0.95	0.46	0.60	0.33
PERSIANN	9.3	1.9	0.98	0.50	0.55	0.28

Figure 4.5 shows the scatter plot of the CMORPH rainfall estimates versus gauge data at pixel level for the 2005/2006 rainfall season. The maximum area average rainfall estimated by CMORPH and recorded by the gauge was 13.6 mm (on 7/1/2006) and 5.9 mm (on 8/1/2006), respectively. It can be observed that there was generally a good agreement between the two methods shown by coefficient of determination (R^2 = 0.6279, n = 178 days). The CMORPH method shows mean absolute error of 3.6 mm/day and root-mean square error of 7.3 mm/day.
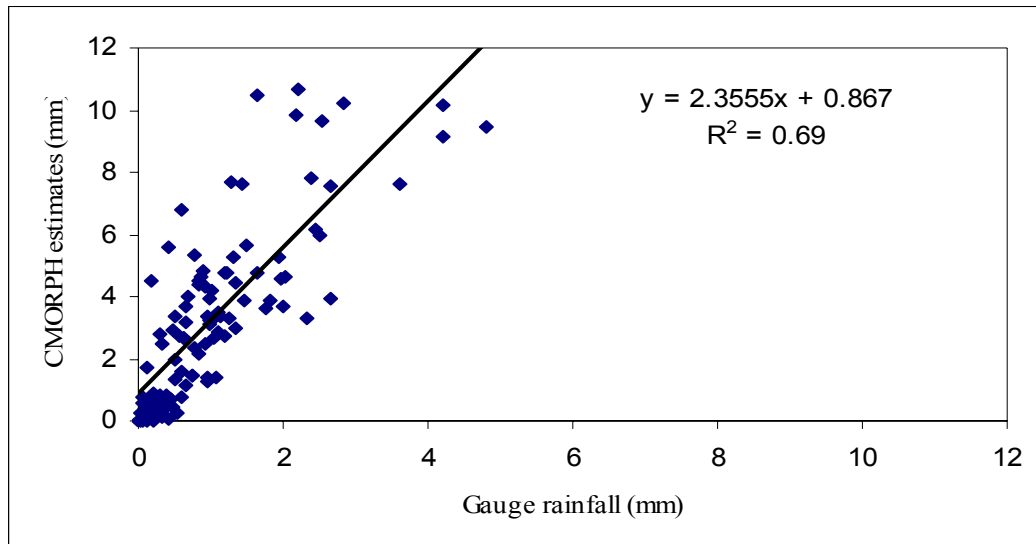

Figure 4.5: Relationship between daily area average CMORPH estimates and gauge data

The relationship between the MPA satellite estimates and gauge data at pixel level for the 2005/2006 rainfall season is shown in Figure 4.6. The maximum area average rainfall estimated by MPA and recorded by the gauge was 11.9 mm (on 6/1/2006) and 5.9 mm (on 8/1/2006, respectively. There was generally good agreement between the two methods as shown by coefficient of determination (R^2 = 0.6337, n = 178 days). The technique is associated with mean absolute error of 5.2 mm/day and root-mean square error of 6.9 mm/day.
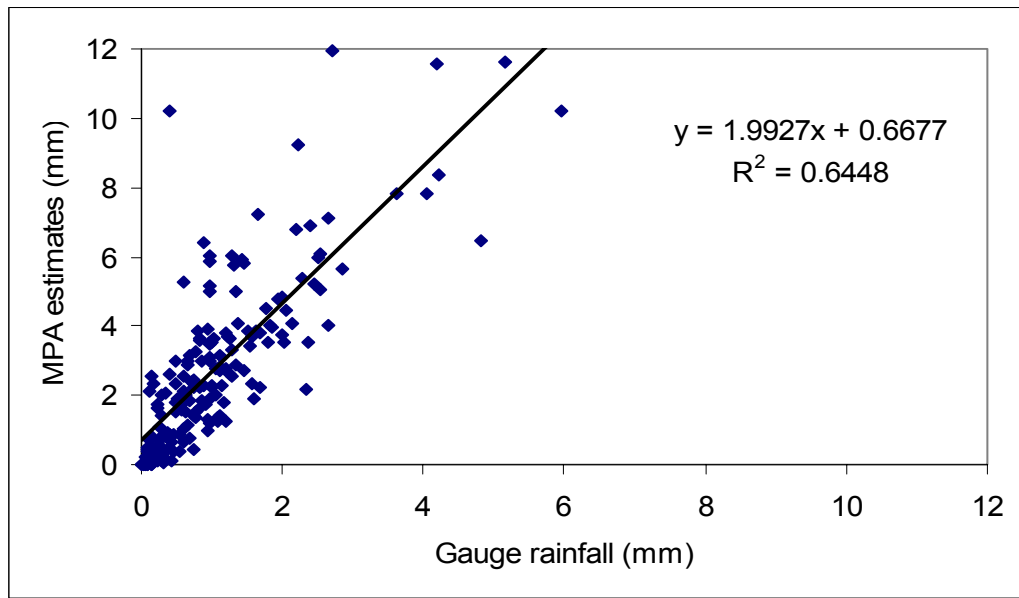
Figure 4.6: Relationship between daily area average MPA estimates and gauge data

The relationship between the NRLB satellite estimates and gauge data at pixel level for the 2005/2006 rainfall season is shown in Figure 4.7. The maximum area average rainfall estimated by NRLB and recorded by the gauge was 14.8 mm and 5.9 mm, (on 8/1/2006), respectively. There was generally a good agreement between the two methods but with slightly lower coefficient of determination (R^2 = 0.6085, n = 105 days) when compared to the CMORPH and MPA algorithms. The method shows the mean absolute error of 3.3 mm/day and root-mean square error of 8.9 mm/day.
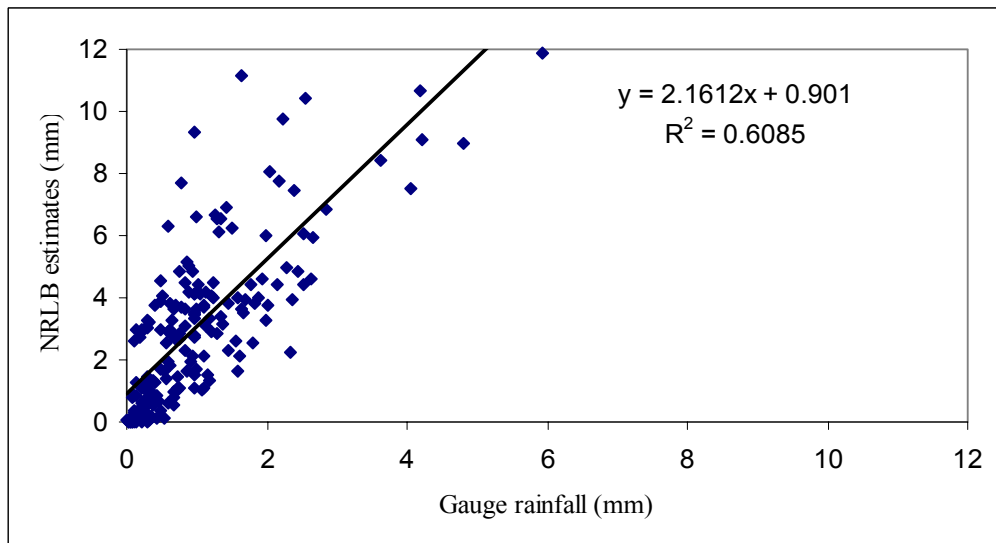

Figure 4.7: Relationship between daily area average NRLB estimates and gauge data

The relationship between the PERSIANN satellite estimates and gauge data at pixel level for the 2005/2006 rainfall season is shown in Figure 4.8. The maximum area average rainfall estimated by PERSIANN and recorded by the gauge was 18.0 mm and 5.9 mm (on 8/1/2006), respectively. There was relatively poor agreement between the two methods as shown by a low coefficient of determination (R^2 = 0.528, n = 176 days). The PERSIANN algorithm exhibit mean absolute error of 2.5 mm/day and root-mean square error of 5.7 mm/day.
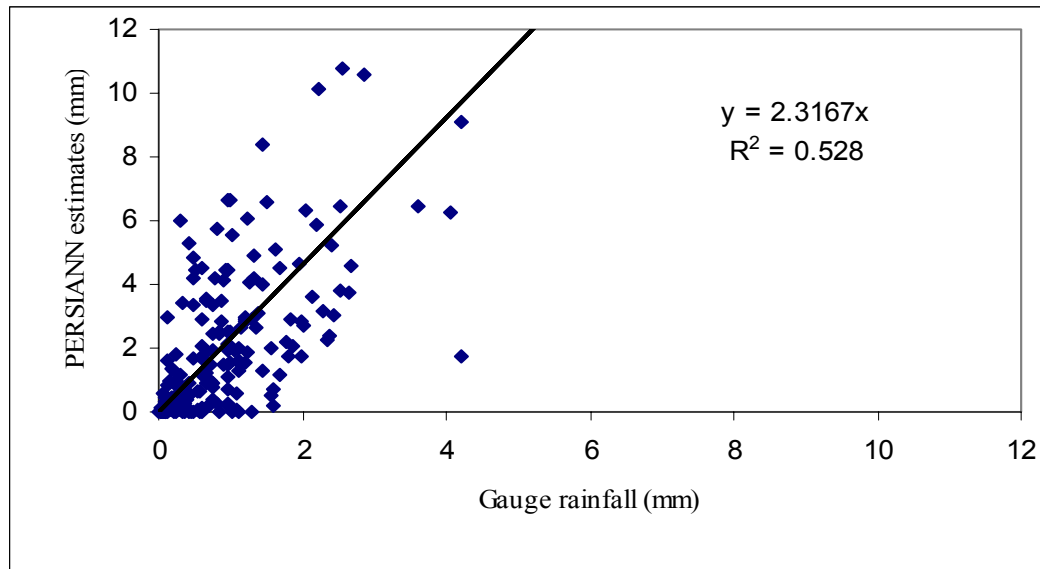

Figure 4.8: Relationship between daily area average PERSIANN estimates and gauge data

Table 4.2 gives the summary of some statistical parameters for the period of 2005/2006. The mean absolute error ranges from 2.5 – 5.2 mm/day and root-mean square error, from 5.7 – 8.9 mm/day. The MPA shows relatively high value of mean absolute error compared to the other methods, while NRLB has relatively high root-mean square error. This is associated with the unavailability of satellite data during the rainfall season. The magnitude of root-mean square errors is acceptable compared with studies carried out in Australia and United States of America. All satellite methods showed positive bias.

Table 4.2: Summary of some statistical parameters for the 2005/2006 rainfall season

Method	Mean absolute error (mm/day)	RMSE (mm/day)	Bias	R^2
CMORPH	3.6	7.3	0.3	0.69
MPA	5.2	6.9	0.4	0.6448
NRLB	3.3	8.9	0.3	0.6085
PERSIANN	2.5	5.5	0.3	0.528

4.1.2   *Comparison between three-daily moving area average and gauge data*

In order to evaluate the improvement of the area average rainfall data, analyses of moving average for three-days were considered. Figure 4.9 shows the relationship between the CMORPH three-daily moving area average estimates and daily area average gauge rainfall. The coefficient of determination ($R^2 = 0.7767$) is considerably higher than the daily area average rainfall.
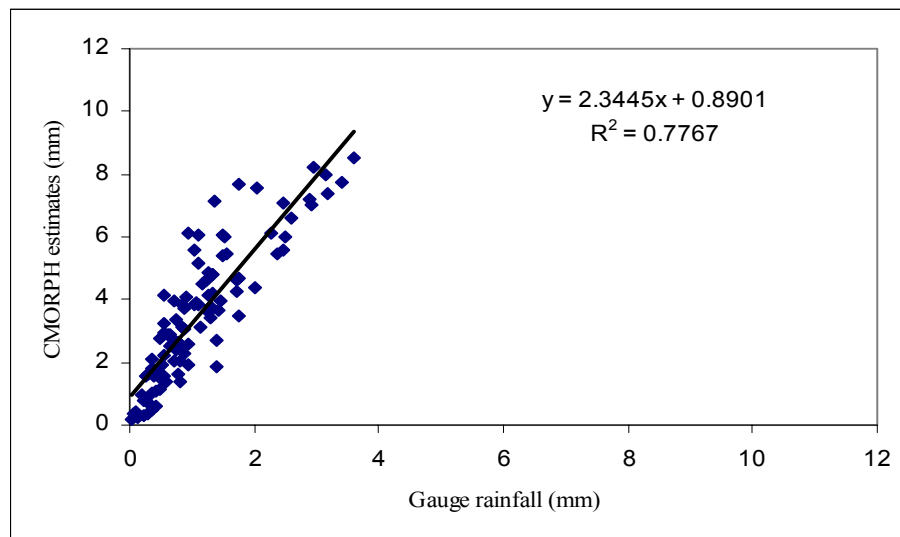

Figure 4.9: Relationship between three-daily moving area average CMORPH estimates and gauge data

Similar improvement was found for the MPA method. After moving the daily area average to three-days, the value of the coefficient of determination increased from 0.6448 to 0.7725. Figure 4.10 shows the relationship between the MPA satellite-based estimation algorithm and gauge rainfall.

$$y = 2.1024x + 0.5508$$
$$R^2 = 0.7725$$
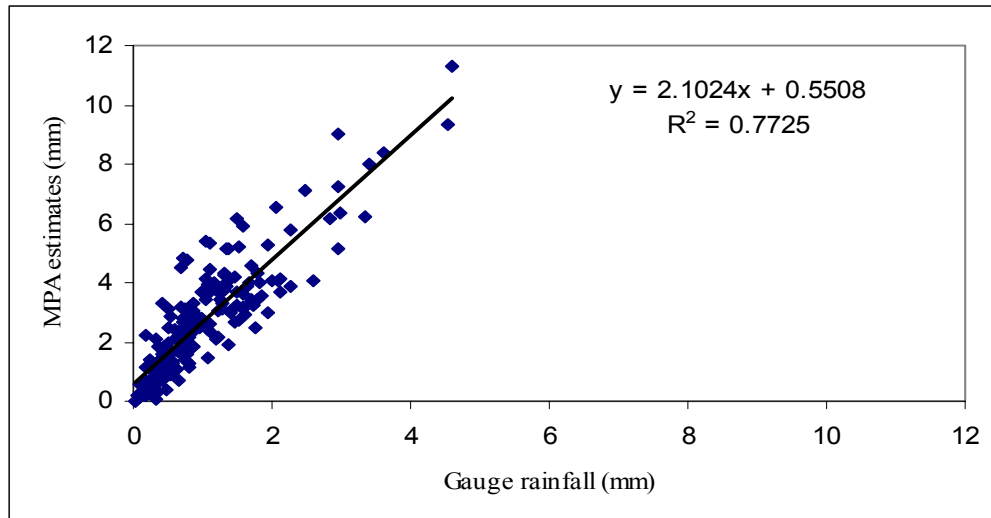
Figure 4.10: Relationship between three-daily moving area average MPA estimates and gauge data

For the NRLB method the value of coefficient of determination for the three-daily moving area average (Fig. 4.11) showed slight difference from the daily area average which was 0.6506 and 0.652, respectively.

$$y = 2.078x + 0.9962$$
$$R^2 = 0.652$$

Figure 4.11: Relationship between three-daily moving area average NRLB estimates and gauge data

Similarly the PERSIANN method also had slightly different coefficient of determination between the three-daily moving area average and the daily area average. The value increased for 0.4016 to 0.5495 (see Fig. 4.8 and 4.12). The summary of the coefficients of determination of the four satellite-based estimation methods correspondent to daily area average and three-daily moving area average are given in Table 4.3.
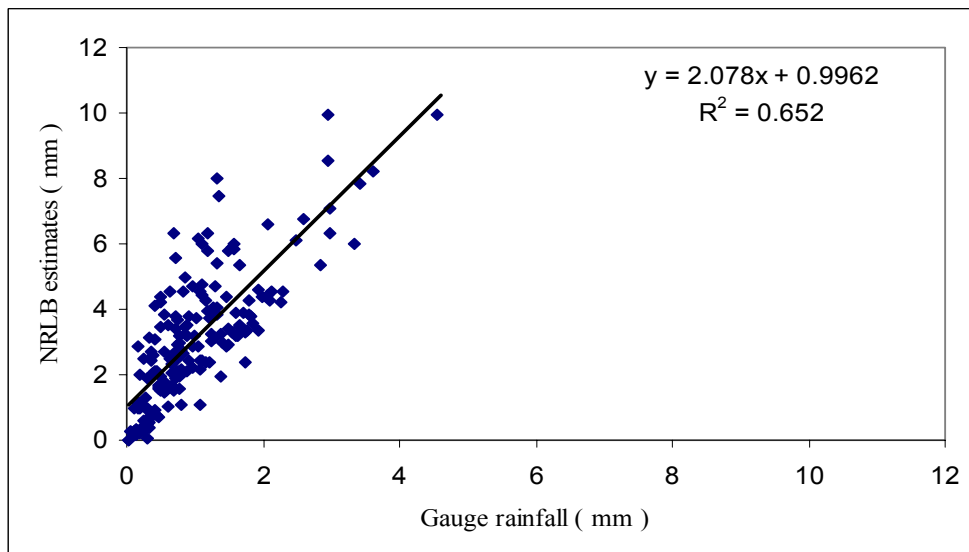

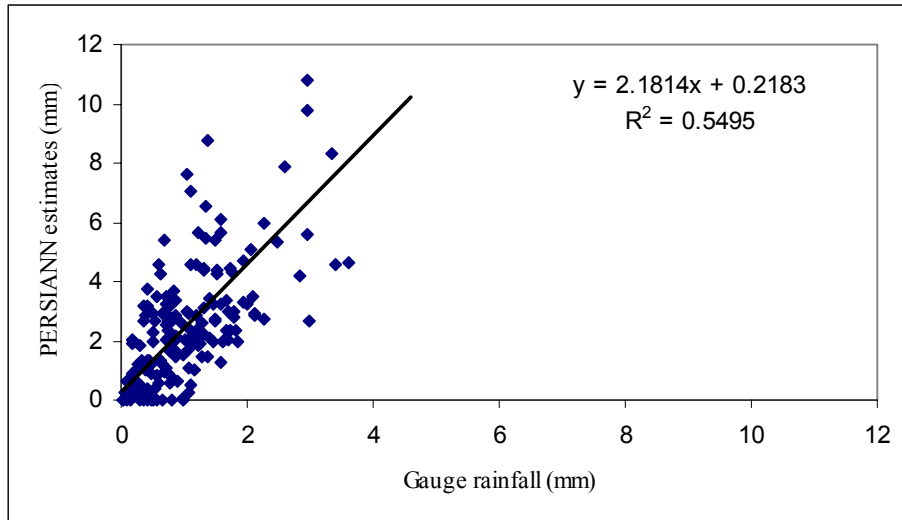Figure 4.12: Relationship between three-daily moving area average PERSIANN estimates and gauge data

Table 4.3: Summary of coefficients of determination

Methods	R^2 before moving the daily area average rainfall	R^2 after three-daily moving area average rainfall
CMORPH	0.69	0.7767
MPA	0.6448	0.7725
NRLB	0.6085	0.652
PERSIANN	0.528	0.5495

4.1.3 Analysis of performance of the algorithms

In order to evaluate the performance of the satellite-based rainfall estimation methods, scatter plots of the critical success index (CSI) between the techniques were plotted. The CSI is a function of both false alarm ratio (FAR) and probability of detection (POD). The values of CSI help to understand and identify which satellite algorithm performed the best. Figure 4.13, shows the linear regression (1:1 linear relationship) between values of CSI obtained using CMORPH and MPA methods. The graph shows that the two methods are highly correlated with coefficient of determination of $R^2 = 0.9652$. This leads to a good performance for the CMORPH and MPA satellite-based estimation methods in the Limpopo Basin.
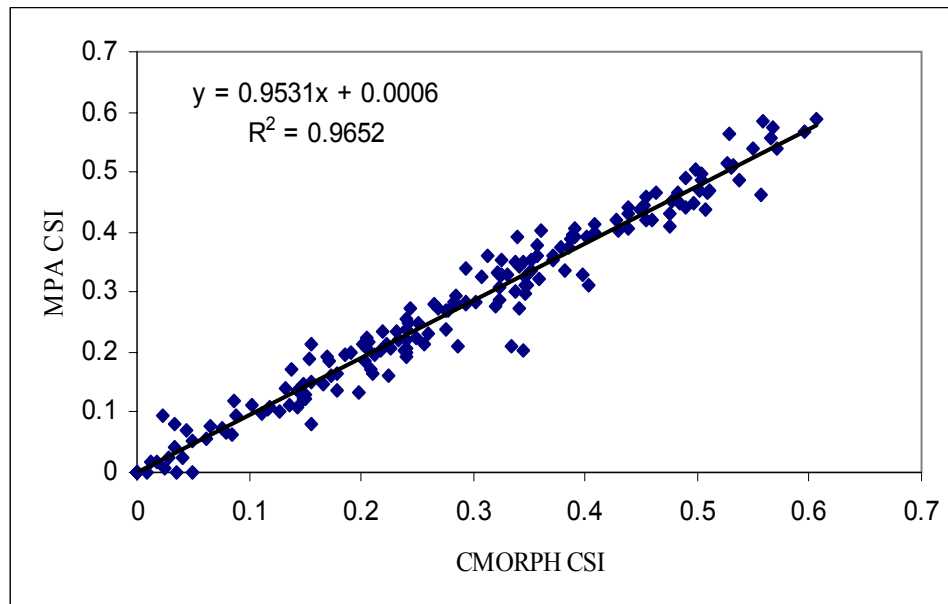
Figure 4.13: Critical success index comparison between CMORPH and MPA for 2005/2006 rainfall season

Similar analysis of the performance of the algorithms was done for CMORPH and NRLB. Figure 4.14, shows the scatter plot of CSI values for the season. There is significant scatter showing very low correlation between the CMORPH and NRLB estimates.

Figure 4.14: Critical success index comparison between NRLB and CMORPH for 2005/2006 rainfall season

Figure 4.15 shows the linear regression between CMORPH and PERSIANN methods. There is also significant scatter showing very little correlation between both techniques.
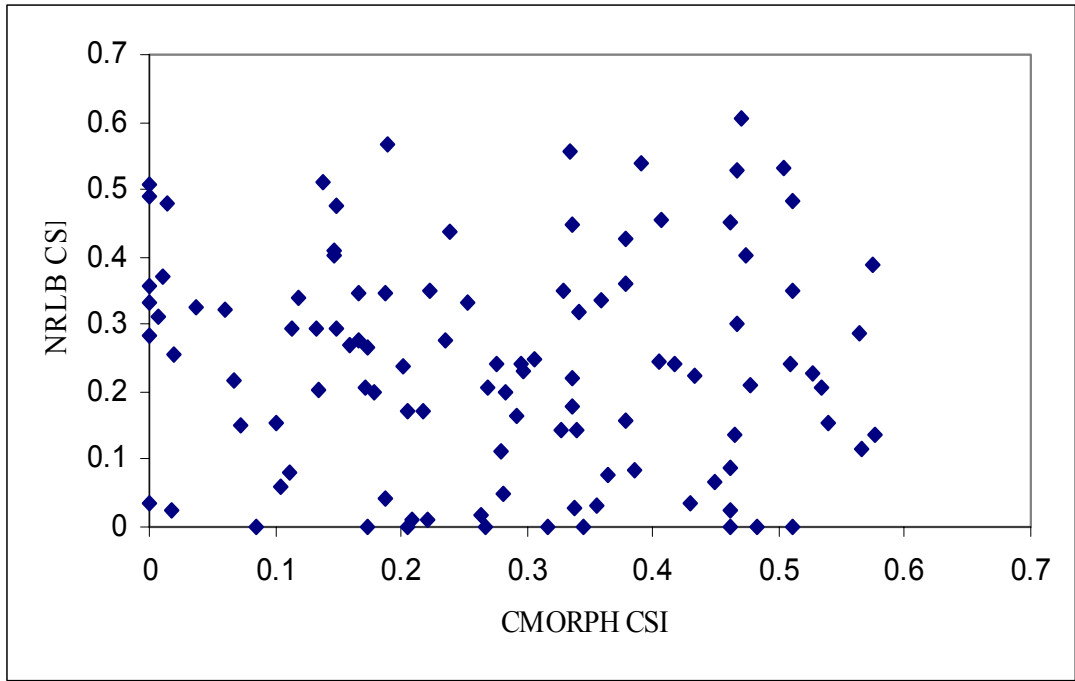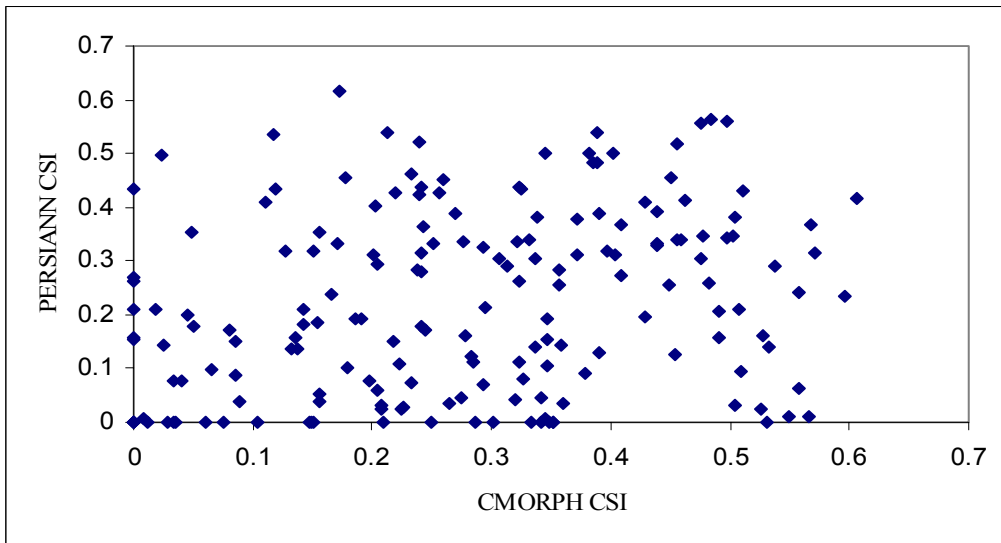

Figure 4.15: Critical success index comparison between PERSIANN and CMORPH for 2005/2006 rainfall season

Table 4.4 shows the summary of the overall performance of the CMORPH, MPA, PERSIANN, and NRLB satellite estimation algorithms, for the six months (October 2005 to March 2006).

Table 4.4: Summary of statistical parameters for the estimation algorithms for all rainfall season of 2005/2006

Method	POD	FAR	ETS	HKS	HSS
CMORPH	0.91	0.19	0.90	0.29	0.28
MPA	0.89	0.17	0.88	0.26	0.26
PERSIANN	0.89	0.18	0.83	0.21	0.21
NRLB	0.76	0.17	0.60	0.23	0.19

It can be seen from the table that CMORPH has high values of POD and FAR compared to the other methods. The POD and FAR values range from 0.76 – 0.91 and 0.17 – 0.19, respectively. CMORPH and MPA exhibit slight differences between the values of skill scores (ETS, HKS and HSS). The two algorithms compared best with the gauge analysis over the Limpopo Basin in most of the statistics. The HSS shows the fraction of correct estimates after eliminating those that would have been correct due purely to random chance. The overestimation of rainfall (from high values of bias) leads the four algorithms having a greater POD and FAR meaning that there is good agreement between gauge and satellite estimates during the rainfall season . The dry conditions observed during the rainfall season of 2005 / 2006 contributed to the high values of FAR because the algorithms tended to over-predict the rainfall.

4.2   Discussions

At the daily scale the CMORPH ($R^2 = 0.69$, n = 178 days) and MPA ($R^2 = 0.6448$, n = 178 days) satellite-based estimation algorithms showed the highest values of coefficient of determination, followed by NRLB ($R^2 = 0.6085$, n = 105 days), and PERSIANN ($R^2 = 0.528$, n = 176 days). This shows relatively good agreement between the CMORPH, MPA and NRLB with gauge rainfall and fair agreement between the PERSIANN and gauge rainfall.

Results of three-daily moving area average rainfall for the four satellite-based estimation algorithms showed improvement of coefficients of determination (R^2) values when compared with three-daily area average gauge rainfall. The values for CMORPH and MPA techniques increased from 0.69 to about 0.7767, and from 0.6448 to 0.7725, respectively, NRLB from 0.6085 to 0.652 and finally, for PERSIANN, from 0.528 to 0.5495. The improvement in the coefficient of determination means that the temporal resolution of three days contributed for the accuracy of the satellite algorithms.

All satellite-based estimation methods overestimate the variance of the recorded gauge amounts. This is demonstrated by the values of positive bias. This is largely as a result of comparing rain gauge point estimates of rainfall to satellite estimates averaged over at least 25 km^2. Scofield (1987), Rosenfeld and Mintz (1988) and more recently McCollum *et al.* (2001) in their studies found also the positive bias between gauge measurements and satellite estimates in semi-arid regions. They attributed the positive bias to the significant evaporation which occurs in semi-arid regions between the cloud base and surface, before the precipitation reaches the ground.

The MPA technique shows a significantly high value of mean absolute error (mean absolute error = 5.2 mm/day), relative to CMORPH, NRLB and PERSIANN. The NRLB shows a high value of root mean square error (RMSE = 8.9 mm/day), relative to the other methods. These errors are associated with the poor rain gauge network coverage in the study area, while the gauge observations may also be a significant source of scatter. For example only three rain gauges were used in southern Zimbabwe an area of about 66070 km^2. The satellite algorithms are also sources of errors since they are indirect methods of rainfall estimation. The satellite sources of errors include the instrument calibration, the conversion retrieval to rain rates and also temporal sampling.

These results show that the methods are better than in identifying raining from non raining grid cells in the Limpopo basin. It can also be seen from value of the bias that all four methods tend to overestimate rainfall (bias > 1). The high value of bias for CMORPH leads to the method having a greater probability of detection (POD) and false alarm ratio (FAR).

The average value of critical success index (CSI) during the rainfall season was 0.28 for CMORPH, 0.27 for MPA, 0.24 for NRLB and 0.22 for PERSIANN. These results show that CMORPH and MPA have good correlation and performed better than the PERSIANN and NRLB algorithms. The PERSIANN and NRLB algorithms are not using passive microwave data from DMSP, and it could be influenced in the performance of these two algorithms.

The Heidke skill score (HSS) shows the success of the algorithm relative to using the mean observed rainfall as the estimate. A value of 0 indicates that the estimates are equivalent to using the mean observed values, whereas a value of 1 indicates perfect match of the observations. Any value greater than 0 therefore indicates the method is skilled. In this case, the result from the four algorithms shows values ranging from 0.21 to 0.28 (see Table 4.2), meaning that all methods are skilled, but the results for CMORPH and MPA are better than PERSIANN and NRLB. CMORPH method outperforms the other three algorithms in almost every validation statistics, for the entire validation period.

Similar results of skill were found by Joyce *et al.* (2004), when comparing the performance of CMORPH method and infrared and passive microwave combined methods, in the USA and Australia. The skill range was between 0.37 – 0.42 in USA, and from 0.26 – 0.36 in Australia.

Chapter 5   CONCLUSIONS and RECOMMENDATIONS

5.0   Introduction

Deriving accurate estimates of rainfall from satellite data at local scale and for short periods of time has long been a major problem in remote sensing. Techniques based on infrared data often rely on space/time averaging to ensure accuracy. Those on passive microwave data are limited to either instantaneous estimates or longer term averages such as monthly periods (Barrett and Beaumont, 1994). Satellite estimates from any specific system have uncertainties but they are improving. Combined estimates from different methods and systems reduce uncertainties and offer the best representation of precipitation in global scale. In this study, Four satellite rainfall estimation methods namely the Climate Prediction Centre Morphing (CMORPH), Multiple Precipitation Analysis (MPA), Precipitation Estimates from Remotely Sensed Information using Artificial Neural Networks (PERSIANN) and Naval Research Laboratory Blended (NRLB) that combine infrared data from Meteosat-8 satellite and passive microwave data from NOAA, DMSP, and TRMM satellites were used and validated against daily rain gauge data over the Limpopo basin, for 2005/2006 rainfall season. The validation was done by comparing satellite-based rainfall estimates with areal average rainfall measured by 90 rain gauges distributed across the basin. This section presents conclusions of the study and suggests some recommendations for further study.

5.1   Conclusions

This study leads to the following conclusions:

- All the four methods showed some skill in estimating rainfall. There was relatively good agreement between CMORPH, MPA and NRLB algorithms and fair agreement between the PERSIANN algorithm and rain gauges. At the daily scale the CMORPH ($R^2 = 0.69$) and MPA (($R^2 = 0.6448$) algorithms showed the highest values of coefficient of determination, followed by NRLB ($R^2 = 0.6085$) and PERSIANN ($R^2 = 0.528$).
- The CMORPH and MPA performed better than PERSIANN and NRLB, according to the critical success index.

- The performance of the satellite-based estimation methods improved when three-daily moving area average rainfall was compared with three-daily area average gauge rainfall. The values increased from 0.69 to about 0.7767 for CMORPH and from 0.6448 to 0.7725. The values for NRLB increased from 0.6085 to 0.652 and finally, for PERSIANN, from 0.528 to 0.5495. The improvement in the coefficient of determination means that the algorithm accuracy increased with time;

- All the algorithms overestimated rainfall in quantity and spatially over the region, and this is a persistent feature of all algorithms with values of positive bias;

- The dry conditions experienced during the 2005/2006 rainfall season could have affected the quality of rain gauge data and contributed negatively to the validation of satellite-based rainfall estimation algorithms because the satellite algorithms tended to over-predict rainfall.

5.2   Recommendations

The validation results for satellite rainfall estimation using the combined infrared and passive microwave methods in the Limpopo Basin, can improve if the rainfall measurement infrastructure and data exchange within the Limpopo Basin between the four countries improved. A similar study should be done during more rainfall seasons in order to improve the accuracy of estimated rainfall and should be extended to other river basins such as Save and Zambezi.

The use of weather radar could greatly contribute to improved rainfall estimation.

REFERENCES

Adler, R. F., and R. A. Mack, 1984: Thunderstorm cloud height rainfall rate relations for use with satellite rainfall estimation techniques. *J. Climate Appl. Meteor.*, **23**, 208 – 296.

Adler, R. F., and A. J. Negri, 1988: A satellite infrared technique to estimate tropical convective and stratiform rainfall. *J. Climate Appl. Meteor.*, **27**, 30 – 51.

Adler, R. F., P. R. Keehn, and I. M. Hakkarinen, 1993: Estimation of monthly rainfall over Japan and surrounding waters from a combination of low-orbit microwave and geosynchronous IR data. *J. Appl. Meteor.*, **32**, 335 – 356.

Adler, R. F., C. Kidd, G. Petty, M. Morrisey, and M. H. Goodman, 2001: Intercomparison of global precipitation products: The Third Precipitation Project (PIP-3). *Bull. Amer. Meteor. Soc.*, **82,** 1377 – 1396.

Ahrens, C. D., 2000: *Meteorology Today*. An Introduction to Weather, Climate and the Environment. Sixth Edition.USA: Brooks/Cole.

Aires, F. C., Prigent, W. B. Rossow, and M. Rothstein, 2001: A new neural network approach including first guess for retrieval of atmospheric water vapour, cloud liquid water path, surface temperatures and emissivities over land from satellite microwave observations. *J. Geophys. Res.*, **106** (D14), 14887 – 14907.

Arkin, P.A., and J. E. Janowiak, 1993: *Tropical and Subtropical Precipitation*. In Atlas of Satellite Observations related to Global Change. England: Cambridge University Press.

Arkin, P. A., and B. N. Meisner, 1987: The relationship between largescale convective rainfall and cold cloud over the Western Hemisphere during 1982–84. *Mon. Wea. Rev.,* **115,** 51 – 74.

Atlas for Disaster Preparedness and Response in the Limpopo Basin, 2003: (CD – ROM). Republic of Mozambique.

Ba, M. B., and A. Gruber, 2001: GOES Multispectral Rainfall Algorithm (GMSRA). *J. Appl. Meteor.*, **40**, 1500 – 1514.

Barrett, E. C., 1970: The estimation of monthly rainfall from satellite data. *Mon. Wea. Rev.,* **98,** 322 – 327.

Barrett, E.C., and D. W. Martin, 1981: The *use of Satellite Data in Rainfall Monitoring*. New York. Academic Press.

Barrett, E. C., C. C. Kidd, and J.O. Bailey, 1988: The Special Sensor Microwave/ Imager: A new instrument with rainfall monitoring potential. *Int. J. Remote Sens.,* **9**, 1943 – 1950.

Barrett, E. C., and M. J. Beaumont, 1994: Satellite rainfall monitoring: an overview. *Rem. Sen. Rev*. **11**, (1 - 4), 49 – 60.

Bellerby, T., M. Todd, D. Kniveton, and C. Kidd, 2000: Rainfall estimation from a combination of TRMM precipitation radar and GOES multispectral satellite imagery through the use of an artificial neural network. *J. Appl. Meteor.*, **39**, 2115-2128.

Borneman, R., 1988: Satellite rainfall estimating program of the NOAA/NESDIS Satellite Analysis Branch. *Natl. Wea. Dig.,* **13** (2), 7 – 15.

Boroto, R. A. J., 2000: *Limpopo River:* Steps Towards Sustainable and Integrated Water Resources Management. Department of Water Affairs and Forestry. South Africa, Pretoria.

Dennett, M. D. 1987: Variation of rainfall – the background to soil and water management in dryland regions. Soil Use and Man., **3** (2), 47 – 57.

Ebert, E. E., A. P. Arkin, R. J. Allam, G. E. Holpin, and A. Gruber, 1996: Results from the GPCP algorithm intercomparison program. *Bull. Amer. Meteor. Soc.*, **77**, 2875 – 2887.

EUMETSAT, 1998: D*irectory of Meteorological Satellites Apllications.* Coordination Group for Meteorological Satellites (CGMS), EUM BR 08.

EUMETSAT, 2004: MSG Interpretation Guide Version 1.0. (CD – ROM). November 2004

FAO, 2001: *Drought Impact Mitigation and Prevention in the Limpopo River Basin: A Situation Analysis,* FAO Sub-Regional Office for Southern and Eastern Africa, Nairobi.

Ferraro, R. R., and G. F. Marks, 1995: The development of SSM/I rain-rate retrieval algorithms using ground based radar measurements. *J. Atmos. Technol.*, **12**, 755 – 770.

Ferraro, R. R., N. Weng, Grody, and L. Zhao, 2000: Precipitation characteristics over land from the NOAA-15 AMSU sensor. *Geophys. Res. Lett.,* **27,** 2669 – 2672.

Ferraro, R. R., P. Pellegrino, S. Kusselson, M. Turk, and S. Kidder, 2002: Validation of SSM/I and AMSU-derived tropical rainfall potential (TraP) during the 2001 Atlantic hurricane season. *NOAA Tech. Rep*. NESDIS **105**, 43.

Flitcroft, I. D., J. R. Milford, and G. Dugdale, 1989: Relating point area average rainfall in semi-arid West Africa and the implications for rainfall estimates derived from satellite data. *J. Appl. Meteo*., **28,** 252 – 266.

Follansbee, W. A., 1973: Estimation of average daily rainfall from satellite cloud photographs. *NOAA Tech. Memo*. NESS **44**, 39.

Follansbee, W. A., and V. J. Oliver, 1975: A comparison of infrared imagery and video pictures in the estimation of daily rainfall from satellite data. *NOAA Tech. Memo*. NESS **62**, 14.

Griffith, C. G., W. L. Woodley, S. Browner, J. Teijeiro, M. Maier, D. W. Martin, J. Stout, and D. N. Sikdar, 1976: Rainfall estimation from geosynchronous satellite imagery during daylight hours. *NOAA Tech. Rep*. ERL 356 – WMPO 7, Boulder, CO.

Griffith, C. G., W. L. Woodley, P. G. Grube, D. W. Martin, J. Stout, and D. N. Sikdar, 1978: Rain estimates from geosynchronous satellite imagery: Visible and infrared studies. *Mon. Wea. Rev.,* **106,** 1153 – 1171.

Grimes, D. I. F., and M. Diop, 2003: Satellite-based rainfall estimation for river flow forecasting in Africa. Part I. Rainfall estimates and hydrological forecast. *Hydrol. Sci. J.*, **48**, 567 – 584.

Gruber, A., 1973: Estimating rainfall in region of active convection. *J. Appl. Meteor.*, **12**, 110 – 118.

Harries, J. E. (2000): The Geostationary Earth radiation Energy experiment: Status and Science. Proceedings of the 2000 EUMETSAT Meteorological Satellite Data User's Conference, Bologna, EUM-P29, 62 – 71.

Hsieh, W. W., and B. Tang, 1998: Applying neural network models to prediction and data analysis in meteorology and oceanography. *Bull. Amer. Meteor. Soc.*, **79**, 1855 – 1870.

Hsu, k., X. Gao, S. Sorooshian, and H. V. Gupta, 1997: Precipitation estimation from remotely sensed information using artificial neural networks. *J. Appl. Meteor.*, **36**, 1176 – 1190.

Huffman, G. J., R. F. Adler, M. Morrisey, D. T. Bolvin, S. Curtis, R. Joyce, B. McGavock, and J. Susskind, 2001: Global precipitation at one-degree daily resolution from multi-satellite observations. *J. Hydrometeor.*, **2**(1), 36 – 50.

Huffman, G. J., R. F. Alder, E. F. Stocker, D. T. Bolvin, and E. J. Nelkin, 2003: Analysis of TRMM 3-hourly multi-satellite precipitation estimates computed in both real and post-real time: 12th AMS Conf. on Sat. Meteor. And Ocean, 9 - 13 February, Long Beach, CA.

Huffman, J. G., R. F. Adler, D. T. Bolvin, G. Gu, E. J. Nelkin, K. P. Bowman, Y. Hong, E. F. Stocker, and D. B. Wolff, 2007: The TRMM multisatellite precipitation analysis (TMPA): Quasi-global, multiyear, combined-sensor precipitation estimates at fine scales. *J. Hydrometeor.,* **8** (1), 38 – 55.

International Reconstruction Conference. (CD – ROM). Republic of Mozambique and UNDP. Rome, 3 – 4 May, 2000.

Janowiak, J. E., R. J. Joyce, and Y Yarosh, (2000): A real-time global half-hourly pixel-resolution IR dataset and its applications. *Bull. Amer. Meteor. Soc.*, **82**, 205 – 217.

Jobard and Desbois, 1992: Remote sensing of rainfall over tropical Africa using Meteosat infrared imagery: sensitivity to time and space averaging. *Int. J. Remote Sens*, **13**(14), 2683 – 2700.

Joyce, R. J., J. E Janowiak, P.A Arkin, and P Xie, 2004: CMORPH: A method that produces global precipitation estimates from passive microwave and infrared data at high spatial and temporal resolution. *J. Hydrometeor*., **5**, 487 – 503.

Kidd, C., 1999: Results of an infrared/passive microwave rainfall estimation technique. Proc. Remote sensing Society, Cardiff, Wales, United Kingdom, *Remote Sensing Society*, 685 – 689.

Kidd, C., D. R. Kniveton, M. C. Todd, and T. J. Bellerby, 2003: Satellite rainfall estimation using combined passive microwave and infrared algorithms. *J. Hydrometeor (AMS)*, **4**(6), 1088 – 1104.

Kummerow, C., and L. Giglio, (1995): A method for combining passive microwave and infrared rainfall observations. *J. Atmos. Oceanic technol*., **12**, 33 – 45.

Kuo, H. L., 1965: On formation and intensification of tropical cyclones through latent heat release by cumulus convection. *J. Atmos. Sci*., **22**, 40 – 63.

Layberry, R., D. R. Kniveton, M. C. Todd, C. Kidd, and T. J. Bellerby, 2006: Daily precipitation over Southern Africa: A new resource for climate studies. *J. Hydrometeor (AMS)*, **7**(1), 149 – 159.

Lethbridge, M., 1967: Precipitation probability and satellite radiation data. *Mon. Wea. Rev.,* **95**, 487 – 490.

Lindesay, J., 1998: Present Climates of Southern Africa. In *Climates of Southern Africa*. Present, Past and Future. Edited by Hobbs, J. E., Lindesay, J. A., and Bridgman H. A. John Wiley and Sons.

Mafoko, T. D. 1990: Soils and land suitability of the Lobatse area. FAO / UNDP GOB Soil Mapping and Advisory Services Project BOT / 85 /011. Field Doc. 15. Gaborone.

McCollum, J. R., W.F. Krajewski, R.R. Ferraro, and M. B. Ba, 2001: Evaluation of biases of satellite rainfall estimation algorithms over the continental United States. *J. Appl. Meteor., 41,* 1065 – 1080.

Miller, S. W., P. A. Arkin, and R. Joyce, 2001: A combined microwave/infrared rain rate algorithm. *Inte. J. Remote Sens*., **22**, 3285 – 3307.

Pan, P., and M. Barnsley, 1999: Remote Sensing Society. Earth Observation from Data to Information. RSS99.

Petty, G., and W. F. Krajewisk, 1996: Satellite estimation of precipitation over land: *Hydrol. Sci*. J., **41**, 433 – 451.

Rao, P. K., S. J. Holmes, R. K. Anderson, J. S. Winston, and P. E. Lehr, 1990: *Weather Satellites*: *System, Data, and Environmental Applications*. *American Meteorological Society*, Boston.

Rosenfeld, D., and Y. Mintz, 1988: Evaporation of rain falling from convective clouds as derived from radar measurements. *J. Appl. Meteor.,* **27**, 209 – 215.

Sanilders, F. L. 1991: Rainfall monitoring based on Meteosat data – A comparison of techniques applied to the Western Sahel. *Int. J. Remote Sens.,* **12** 1331 – 1347.

Schmetz, J. P. Pili, S. Tjemkes, D. Just, J. Kerkmann, S. Rota, and A. Ratier, 2002: An Introduction to Meteosat Second Generation (MSG). *Bull Amer. Meteor. Soc*., **83**, 977 – 992.

Schulze, R. E. 1997: South African atlas of agro-hydrology. Report TT82/96. Pretoria. Water Research Commission.

Scofield, R. A. V. J., and Oliver, 1977: A Scheme for estimating convective rainfall from satellite imagery. *NOAA Tech. Memo*. NESS **86**, Washington D. C.

Scofield, R. A., 1987: The NESDIS operational convective precipitation estimation technique. *Mon. Wea. Rev.,* **115,** 1773 – 1792.

Scofield, R. A., and R. J. Kuligowski, 2003: Status and outlook of operational satellite precipitation algorithms for extreme-precipitation events. *Weather and Forecasting*, **18**, 1037 – 1050.

Sorooshian, S., K. L. Hsu, X. Gao, H. V. Gupta, B. Imam, and D. Braithwaite, 2000: Evaluation of PERSIANN system satellite-based estimates of tropical rain. *Bull. Amer*. *Meteor. Soc*., **81**, 2035 – 2046.

Spayd, L. E., and R. A. Scofield, 1984: A tropical cyclone precipitation estimation technique using geostationary satellite data. *NOAA Tech. Memo*. NESDIS **5**, 36.

Spencer, R. W., 1986: A satellite passive 37 GHz scattering-based method for measuring oceanic rain rates. *J. Climate Appl. Meteor*., **25**, 754 – 766.

Spencer, R. W., H. M. Goodman, and R. E. Hood, 1989: Precipitation retrieval over land and ocean with the SSM/I: Identification and characteristics of the scattering signal. *J. Atmos. Oceanic Technol.,* **6,** 254 – 273.

Stanley, Q. K., and H. V. Thomas, 1995: *Satellite Meteorology*. An Introduction. United Kingdom. Academic Press.

Stephenson, D. B., 2002: *Glossary of Forecast Verification Terms*. Wiley and Sons Ltd.

Stout, J.E., W. D. Martin, and D. N. Sikdar, 1979: Estimating GATE rainfall with geosynchronous satellite images. *Mon. Wea. Rev*., **107**, 585 – 598.

Tsintikidis, D., J. L. Huferman, N. Anagnostou, W. F. Krajewski, and T. F. Smith, 1997: A neural network approach to estimating rainfall from spaceborne microwave data. IEEE Trans. *Geosci. Remote Sens*., **35**, 1079 – 1092.

Turk, F. J., J. Hawkins, E. A. Smith, F. S. Marzano, A. Mugnai, and V. Levizzani, 2000: Combining SSM/I TRMM and infrared geostationary satellite data in a near- real time fashion for rapid precipitation updates: Advantages and limitations. Proc. 2000.

Turk, F. J., E. E. Ebert, O. J. Oh, B. J. Sohn, V. Levizzani, E. A Smith, and R. R Ferraro, 2003: Validation of an operational global precipitation analysis at short time scales. 12th AMS Conf. on Sat. Meteor. And Ocean, 9-13 February, Long Beach, CA.

Vicente, G. A., R. A. Scofield, W. P. Menzel, 1998: The operational GOES infrared rainfall estimation technique. *Bull. Amer. Meteor. Soc.*, **79**, 1883 – 1898.

Vicente, G. A., J. C. Davenport, and R. A. Scofield, 2001: The role of orographic and parallax correction on real time high resolution satellite rain rate distribution. *Inte. J. Remote Sens.*, **23**, 221 – 230.

Visser, P. J. M, D. Dicks, I. T. H. Deyzel, and G. G. S. Pegram, 2004:*Radar and Satellite Products*. Spatial Interpolation and Mapping of Rainfall (SIMAR). WRC report No.1152/1/04.

Weinman, J. A., and P. J. Guetter, 1977: Determination of rainfall distributions from microwave radiation measured by the *Nimbus 6* EMSR. *J. Appl. Meteor.,* **16,** 437 – 442.

Wylie, D. P., 1979: An application of geostationary satellite rain estimation technique to an extratropical area. *J. Appl. Meteor.*, **18**, 1640 – 1648.

WMO, 1996: *Guide to Meteorological Instruments and Methods of Observations*. Sixth Edition. WMO No.8.

Woodley, W. L., C. G. Griffith, J. S. Griffin, and S. C. Stromatt, 1980: The inference of GATE convective rainfall from SMS - 1 imagery. *J. Appl. Meteor.*, **19**, 388 – 408.

www.eumetsat.org/WEBBOPS/msg_interpretation/powerPoints/Channels/Schmetz7july.doc. Accessed on 20 May 2007.

www.msi.umn.edu/software/idl/tutorial-9k. Accessed on 15 May 2007.

Xu, L., X. Gao, S. Sorooshian, P. A. Arkin, and B. Imam, 1999: A microwave infrared threshold technique to improve the GOES precipitation index. *J. Appl. Meteor.*, **38**, 569 – 579.

Yilmaz, K. K., T. S. Hogue, H. Hsu, S Sorooshian, H. V. Gupta, and T. Wagener, 2005: Intercomparison of rain gauge, radar, and satellite-based precipitation estimates with emphasis on hydrologic forecasting. *J. Hydrometeor. (AMS),* **6** (4), 497 – 517.

APPENDIX

Appendix I: *Statistical parameters used in validation process*

Statistical parameter	Definition	Range
Mean Error or BIAS	$BIAS = \frac{1}{N}\left[\sum_{I=1}^{N}\left(E_i - O_i\right)\right]$	0 to 1
Root Mean Square Error	$RMSE = \left[\frac{1}{N}\sum_{i=1}^{N}\left(E_i - O_i\right)^2\right]^{\frac{1}{2}}$	0 to 1
Correlation coefficient	$R^2 = \dfrac{\left[\sum_{i=1}^{N}\left(E_i - \overline{E}_i\right)\left(O_i - \overline{O}_i\right)\right]^2}{\sum_{i=1}^{N}\left(E_i - \overline{E}_i\right)^2 \cdot \sum_{i=1}^{N}\left(O_i - \overline{O}_i\right)^2}$	-1 to 1
Probability of detection	$POD = \dfrac{h}{h + m}$	0 to 1
False Alarm Ratio	$FAR = \dfrac{h}{h + f}$	0 to 1
Critical Success Index	$CSI = \dfrac{h}{h + m + f}$	0 to 1
Equitable Threat Score	$ETS = \dfrac{h - h_{random}}{h + m + f - h_{random}}$	-1/3 to 1
Hanssen and kuipers Score	$HKS = \dfrac{h}{h + m} - \dfrac{f}{f + z}$	-1 to 1
Heidke Skill Score	$HSS = \dfrac{h}{h + f + m}$	-1 to 1

Where:

$$h_{random} = \frac{(h + m)(h + f)}{h + m + f + z}$$

O_i= represents the i-th observation
E_i= represents the i-th estimation
N= series of estimation